UNIVERSITY OF CALIFORNIA,
IRVINE

In Vitro Tools for Quantifying Structure–Function Relationships in Cardiac Myocyte Cells and Tissues

THESIS

submitted in partial satisfaction of the requirements
for the degree of

MASTER OF SCIENCE

in Biomedical Engineering

by

Meghan Brianne Knight

Thesis Committee:
Assistant Professor Anna Grosberg, Chair
Associate Professor Elliot L. Botvinick
Professor William Tang

2015

TABLE OF CONTENTS

LIST OF FIGURES

LIST OF TABLES

ACKNOWLEDGMENTS

I would like to thank my committee members and committee chair for their support and guidance throughout this process. Their mentorship and advice has been critical to my journey. I would also like to recognize and thank Dr. Botvinick for helping us to formulate the title of my paper and first chapter.

I would also like to thank the BEAMS lab at UC, Irvine for aiding in the confocal imaging used in this work with particular recognition of Abishek Kurup, Mark Keating, Shreyas Raj Ravindranath, and Thi Nha Timothy Tran. Additionally, I also thank Kelsey Fung for helping to establish the qPCR work used in this paper. I also thank Linda McCarthy for her contributions to the confocal imaging and for her outstanding work as a lab manager in the core facility where the cell culture work for this thesis was completed. I would also like to thank Nancy Drew for helping me with the computational modeling used in this paper. I thank my lab mates Danny Baldo Jr., Nancy K. Drew, and Nicholas Johnsen for all of the great memories I shared with you during our time together. Last, I thank my family and friends for their unwavering support of my education and career goals. I would not be where I'm at without any of you!

I thank Elsevier for permission to include copyrighted photographs and text as Chapters one and two of my thesis. I also thank Springer International Publishing for permission to include the introduction of my thesis, which was originally published in Linguistics Journal. Financial support was provided by the National Science Foundation EAGER award (Award Number 1338609).

ABSTRACT OF THE THESIS

In Vitro Tools for Quantifying Structure–Function Relationships in Cardiac Myocyte Cells and Tissues

By

Meghan Brianne Knight

Master of Science in Biomedical Engineering

University of California, Irvine, 2015

Assistant Professor Anna Grosberg, Chair

The heart is a complex organ whose structure and function are intricately linked at multiple length scales. Though several advancements have been achieved in the field of cardiac tissue engineering, current *in vitro* cardiac tissues do not fully replicate the structure or function necessary for effective cardiac therapy and cardiotoxicity studies. This is partially due to a deficiency in current understandings of cardiac tissue organization's potential downstream effects, such as changes in gene expression levels. We developed a novel *in vitro* tool that can be used to decouple and quantify the contribution of organization and associated downstream effects to tissue function. To do so, cardiac tissues were designed to be organized anisotropically on a local scale and with any desired organization on a global scale. This study's results showed that if the downstream effects were muted, the relationship between developed force and tissue organization was a surprisingly simple sum of force pseudovectors. Thus, a quantitative tool was developed to predict the generated stress based on organization. Furthermore, it was demonstrated that the tool could be used to estimate the changes in stress production due to downstream effects decoupled from tissue architecture. This has the potential to elucidate properties coupled to tissue architecture, which change force production and pumping function in the diseased heart or stem-cell derived tissues.

Introduction

The electrical and mechanical function of multicellular cardiac tissues is highly dependent on the structure of the tissue. In recent decades, new experimental techniques have been developed to study tissue-level interactions between structure and function *in vitro*. These experiments have revealed that mimicking the anisotropic structure of healthy heart tissue is essential to fully recapitulating a functioning myocardium, which is a complex and challenging task.

Organization and structure *in vivo* and *in vitro*

Structural remodeling of cardiac tissue is evident in many heart diseases, which contributes to functional declines. Two common types of remodeling are seen in the heart: hypertrophy and dilation. Hypertrophy is characterized by thickening of the ventricle walls associated with a disorganization of myocardial tissue. Dilation is characterized by a thinning of the ventricle walls and is also associated with changes in myocyte structure [1, 2]. Significant regional anatomical remodeling, such as sarcomere disorganization and fibroblast infiltration, can be seen in failing hearts when compared to healthy hearts, further supporting the concept that the structural organization of the heart at multiple scales is important to proper cardiac function [3, 4]

To determine how the microscopic organization of cardiac tissue affects its physiological function, several techniques have been developed to control the architecture of cardiac tissues *in vitro*. One technique is microcontact printing, where myocytes are seeded onto elastic polymer substrates micropatterned with extracellular matrix proteins, such as fibronectin, which induces them to grow along the protein pattern [5, 6]. A second approach to patterning is to use external topographical cues. Studies have shown that cardiac myocytes organize anisotropically on PDMS scaffolds with repeating ridged features [7, 8] or microgrooved hydrogel substrates [9, 10]. To mimic the multi-scale nature of the heart, other research has produced topographical cues with

features that range from micro- to nano-scale by using wrinkled shrink-wrap films as culture substrates [11]. A final technique to guide organization of cardiac tissue is mechanical stretching. *In vitro,* cardiac myocytes seeded onto thin PDMS substrates that are cyclically stretched for at least 24 hours orient along the direction of stretch [12, 13]. Thus, several techniques can be used to mimic the architecture of healthy or diseased cardiac tissues *in vitro*, allowing investigators to study how tissue structure regulates function in a controlled setting.

Although 2D monolayers are helpful for understanding the function of sheets of heart tissue, engineering more complex three dimensional (3D) tissues is also important for revealing mechanisms of cardiac disease. However, appropriate 3D scaffolds must provide structural and physiological characteristics that mimic that of the heart *in vivo.* Vascularized cardiac tissue constructs formed by seeding synthetic polylactic acid/poly(lactic-*co*-glycolic acid) (PLLA/PLGA) porous scaffolds with cardiac myocytes derived from human embryonic stem cells (hESC), endothelial cells, and embryonic fibroblasts have been shown to produce electrophysiological functions similar to those seen *in vivo*, but do not recreate the anisotropic architecture of native cardiac tissue [14]. Rotary jet spun scaffolds of nanofibers have been promising 3D constructs with anisotropic features that promote alignment of cardiac myocytes [15], but there is no evidence that these fibers can promote maturation or vascularization. Other studies have shown that electrically pacing neonatal rat cardiac myocytes cultured onto collagen hydrogels produces electrically mature myocytes aligned in the direction of the field lines [16]. However, the dimensions of these constructs are currently limited to the depth of the diffusion of oxygen, although adding fluidic channels to the scaffold has been implemented to improve perfusion [17]. Thus, although synthetic scaffolds are promising, we still lack the technology to engineer 3D cardiac tissues with proper structural and functional properties.

Recently, decellularized hearts have been used as native cardiac ECM scaffolds, which are perfused and repopulated with cardiac myocytes. Decellularized ECM is advantageous because it maintains all of the necessary structural cues of the native heart. Eight days after re-perfusing decellularized hearts with cardiac myocytes, the constructs generate weak pumping function with the aid of electrical stimulation [18]. Though decellularization followed by repopulation is promising, repopulated hearts are insufficiently mature and revascularization is not possible with current methods. Decellularized mouse hearts have also been repopulated with human iPS-derived cardiac myocytes, demonstrating the potential for decellularized cadaver hearts to serve as scaffolds for a patient's own cells [19]. This method would reduce the need for immune suppression after organ transplant. Thus, although engineered 3D cardiac tissues are an attractive "quick fix" to many problems such as heart disease or heart transplant availability, we still do not have the tools to accurately replicate the physiological and mechanical functions of the natural heart.

Tissue organization and electrophysiology

In order to efficiently pump blood, the heart relies on a complex network of electrical signals that activates myocytes to contract and relax in a synchronous, pulsatile pattern [20]. The electrical signals of the heart can be traced *in vivo* via electrocardiography (ECG) [21]. During infarct, reperfusion, or arrhythmia, the electrical activity of the heart becomes abnormal, which can be detected by ECGs [22]. Electrophysiological changes have also been observed in diseased hearts with remodeled cardiac tissue. For example, studies have shown that left ventricular hypertrophy, which is characterized by enlarged myocytes, results in lower conduction velocities [23]. The electrical activity of living hearts can be measured *ex vivo* using Langendorff preparations, where explanted hearts are immediately perfused with nutrient-rich solutions so that

their physiology is preserved outside of the animal's body. Because Langendorff preparation allows the heart to continue functioning, the electrical properties of the heart can be studied using techniques such as optical mapping [24-26]. Optical mapping entails loading a tissue with a voltage sensitive dye, which changes its emission properties based on the membrane potential of the tissue. Thus, action potential propagation can be tracked using cameras equipped for high-speed fluorescent imaging. For example, optical mapping of Langendorff preparations has been used to show changes in electrophysiology with respect to molecular changes in the tissue [27].

Electrical activity within engineered 2D cardiac monolayers can also be visualized with optical mapping by tracking the fluorescence of voltage-sensitive dyes loaded in tissues that are mounted on a microscope [28, 29]. In addition, calcium sensitive dyes can be used to detect calcium transients within cardiac myocytes and their contributions to atypical beating [30]. Using these methods, it has been shown, *in vitro,* that electrophysiological abnormalities depend on tissue organization. For example, cardiac tissue alignment has a significant effect on the electrophysiological properties of the heart, such as action potential duration, conduction velocities, and calcium transients [6-8, 31, 32]. Importantly, aligned tissues have a higher longitudinal conduction velocity, which is likely because action potentials propagate more rapidly through cytoplasm than across cell-cell junctions [33]. These studies indicate that cardiac tissue architecture and electrophysiology are tightly coupled.

Tissue organization and contractility

Cardiac contractility is vital to the function of the cardiovascular system. The contraction of the heart can be analyzed at various scales ranging from the cellular scale to the full organ scale [34]. Changes in heart contractility are usually associated with poor pumping function, which are signs of a diseased heart [21]. Ejection fraction is a measure of the volumetric fraction of blood

leaving the heart with each contraction and is typically 55% or greater during systole in a normal healthy heart [35]. The contraction during systole is characterized by a 14% shortening of the myofibers accompanied by a significant thickening of the heart wall [36]. Additionally, pressure changes within the chambers themselves act as secondary driving forces to transport blood into and out of the chambers, which aids contractility.

Heart disease is highly correlated with changes in contractility, as measured by changes in ejection fraction. For example, hypertrophy, characterized by an enlarged heart, is associated with a decrease in ejection fraction [37]. Using the Langendorff preparations previously mentioned, it has been shown that ischemic hearts have much higher diastolic pressures than healthy, non-ischemic hearts [38]. To begin to understand what factors are contributing to poor function of the diseased heart, studies that elucidate these elements on a smaller scale must first be conducted.

Several methods have been developed to measure the contractility of cardiac tissues *in vitro.* In one method, micron-sized flexible PDMS posts are molded from a silicon wafer and seeded with cardiac myocytes, which displace the posts as they contract. By measuring the displacement of the posts with a high-speed camera, contractile forces generated by the tissue can be calculated [39-41]. Another assay, known as muscular thin films (MTFs), has also been developed to measure the diastolic and peak systolic stresses of monolayers of engineered cardiac tissues [6, 13, 42, 43]. MTFs consist of thin films of PDMS cut into cantilevers and temporarily adhered to a glass coverslip by a temperature-sensitive polymer. The PDMS is micropatterned with fibronectin and seeded with cardiac myocytes to form anisotropic cardiac tissues. After the tissues are cultured for several days, the MTFs are carefully peeled from the glass coverslip, which causes the temperature-sensitive polymer to release the MTF cantilevers from the glass coverslip. MTFs are then paced by electrical stimulation to contract at a specific frequency and MTF curvature is

analyzed to determine the stress produced by the cardiac tissue. The "heart on a chip" technology combines multiple MTFs onto one coverslip to increase throughput [44, 45]. "Heart on a chip" can also be combined with a range of other techniques, such as optical mapping, immunostaining, and drug dose response studies (Fig. 4), to correlate multiple structural and functional parameters. With MTFs and "heart on a chip", it has been shown that the peak systolic stress produced by a tissue is highly dependent on the alignment of the sarcomeres within the tissue [6, 13, 44]. This suggests that organization is a key factor to reproducing viable, functional cardiac tissue *in vitro*, and loss of organization is likely one of the key factors contributing to poor function of diseased hearts. Thus, analyzing both structural and functional properties of engineered cardiac tissues is essential for understanding disease progression in the heart.

Stem cell-derived cardiac tissues: Potential therapeutic applications

Many of the body's tissues and organs are able to repair themselves after injury due to cell proliferation and/or the presence of stem cells that can differentiate and repopulate the site of injury [46, 47]. However, the adult heart has very limited regenerative potential because mature cardiac myocytes are essentially post-mitotic [48] and there is an extremely limited number of cardiac myocyte progenitor cells [49]. Thus, after an infarct, the portion of myocardium that dies is replaced with scar tissue, which greatly impairs the function of the heart [21]. For these reasons, stem cells and stem cell-derived cardiac myocytes are being actively pursued as therapeutic options to repair and regenerate injured myocardium.

One strategy for repairing infarcted myocardium is to inject bone marrow-derived mesenchymal stem cells directly into damaged areas of the heart, with the goal that they will differentiate into cardiac myocytes due to environmental cues. This strategy does promote cardiac regeneration and reduce fibrosis, but only partially recovers the function of the infarcted heart [50].

One major problem with this approach is the retention of stem cells at the transplantation site is very low, as the majority of cells die within the first few days after transplantation [51]. Additionally, there are severe risk factors involved, including the potential for tumor formation or the potential for stem cells to differentiate into cells other than myocytes [52]. Injections of human embryonic stem cell derived-cardiac myocytes have been shown to re-muscularize infarcted primate hearts, although with a high risk of arrhythmias [53]. Thus, using stem cells and stem cell-derived cardiac myocytes to repair damaged myocardium is promising, but still poses tremendous challenges.

Drug testing is another potential application for stem cell-derived cardiac myocytes. Drug failure due to cardiotoxicity is a major burden on the pharmaceutical industry [54] and is partially attributed to the industry's use of animal models or overly-simplified cell culture systems for drug testing, both of which have limited relevance to native cardiac tissue. Thus, a source of fully functional human cardiac myocytes derived from stem cells would resolve problems such as species differences in the behavior of *in vitro* cardiac models [19, 55]. However, while stem cells can be differentiated into cardiac myocytes, these cells are very immature and there is evidence that they retain some non-cardiac myocyte gene expression [56, 57]. Thus, to utilize stem cell-derived cardiac myocytes for drug studies, it is essential to ensure that their *in vitro* function mimics *in vivo* behavior, which can be achieved using the "heart on a chip" assay described above [44]. For example, comparing primary neonatal cardiac myocytes to cardiac myocytes derived from either embryonic or induced pluripotent stem cells (iPSCs) has shown functional deficiencies in both populations of stem cell-derived cardiac myocytes [58]. Quantifying the function of stem cell-derived cardiac myocytes as differentiation protocols improve will help evolve these cells into a usable population of cells useable for predictive drug testing.

In vitro models of cardiac tissue engineered with iPSC-derived cardiac myocytes also have significant potential for personalized medicine. Because iPSCs are typically reprogrammed from patient skin cells or blood cells, iPSC-derived cardiac myocytes have the same genetic background as the patient from which they were isolated and thus they can be expected to respond to drugs similar to the patients' native cardiac myocytes [56, 59]. By combining the "heart on a chip" assay with iPSC-derived cardiac myocytes from patients with genetic diseases, such as inherited cardiomyopathies, researchers can study disease mechanisms in a human-relevant model system and rapidly screen the functional effects of therapies on a patient-by-patient basis [60]. Thus, *in vitro* tools are essential for evaluating stem cell-derived cardiac myocytes and their functional responses to drugs.

Conclusion

The pumping function of the heart is highly dependent on its tissue, cellular, and molecular organization, as well as gene and protein expression [1, 8, 13]. Because structure, function, and gene expression are interconnected, it is difficult to decouple these factors from each other using only *in vivo* systems. Thus, developing and utilizing *in vitro* models that can replicate and decipher these interactions at the molecular, single cell, and/or tissue level will not only help understand how the heart as an organ functions in health and disease, but also lead to the development of biomimetic cardiac tissues that can be used for disease modeling and drug screening. Furthermore, recapitulating cardiac tissue *in vitro* can lead to the development of new therapies such as heart patches or even engineered heart transplants for cardiac diseases such as heart failure, which currently have extremely limited therapeutic options.

Chapter 1

The Resultant Force of a Cardiac Tissue is the Sum of its Parts

As described in the introduction, to effectively pump blood throughout the body, the heart is organized into laminar sheets of cardiac fibers, myofibrils, which consist of sarcomeres - the main force producing units of cardiac muscle [61, 62]. Ideally, each sarcomere produces a contractile force perpendicular to its z-lines and parallel to the actin and myosin fibrils [63]. As a large number of sarcomeres work in synchrony to produce the force necessary for the heart to pump blood, it is essential for them to be properly organized. Accordingly, in the diseased heart, there is evidence of structural remodeling of myofibrils, and thus the force producing units, which is thought to contribute to poor cardiac function [1, 3, 64]. However, the decline in pumping force might not solely be due to changes in force unit organization, but may also be correlated to other downstream effects associated with structural remodeling. Indeed, *in vivo* studies have revealed a correlation between cardiac remodeling, heart disease, and several other factors such as changes in gene expression [65, 66]. The coexistence and interdependence of these factors makes it impossible, with current technologies, to decouple them *in vivo*. *In vitro* studies have been shown to be a more practical method to separate each variable and study the relationship between them.

Several *in vitro* assays have been developed to measure the contractility of engineered cardiac myocyte tissues of varying organization and have the potential to accomplish a decoupling of the factors seen *in vivo* [67-69]. One such technology is the muscular thin film assay, a device made of synthetic polymer films on which cardiac myocytes of isotropic and anisotropic organization have been cultured [42]. Through this assay, it has been shown that contractility of the engineered myocardium is related to the sarcomeric organization of the tissue [6]. However, the relationship

is non-trivial, indicating a presence of other factors that are influencing the dependence. Indeed, other experiments have shown that a change of *in vitro* cardiac tissue organization is also associated with downstream effects such as changes in electrophysiology, gap junction morphology and distribution, and gene expression levels [6, 13, 33, 70, 71]. These downstream effects are likely to further affect the contractility of cardiac tissues. It was shown using a very basic model that the amount of force produced by well-organized cardiac monolayers was approximately twice the expected value based on the force measured in isotropic tissues [6]. However, this model ignores a large number of cardiac tissue properties, such as the dipole nature of sarcomeres, the viscoelastic properties of the cells, and the non-uniform integrin distribution, which makes it impossible to interpret the model's results unless it is validated. Therefore, it is not possible to determine how much of the force difference is due to the downstream effects and how much is directly caused by sarcomere reorganization. To address this, it is imperative to create an experimental platform that decouples the change in tissue organization from the associated downstream effects.

We hypothesized that if the cells are locally organized and globally disorganized, most of the inputs that control the downstream effects will match those seen in an anisotropic tissue, and the global stress would only depend on the physical force vector changes (i.e. sarcomere organization). Thus, we aimed to design a new tissue pattern with parquets of organized tiles combined together to form the desired overall isotropic organization. From these novel tissues, even though it ignored a host of factors, the basic net force model was tested for predictive capabilities. Furthermore, the parquets were assembled into tissues with a range of global organizations, and the basic model was further validated. The results of this study suggest that we have created a technological platform that can be used to quantitatively determine the contribution of downstream effects to

change in force production of engineered muscle tissues at any organization. This is a powerful tool as elucidating these effects has the potential to further current understanding of the consequences of cardiac tissue remodeling in the diseased heart.

Results

In this work, we pursued two goals: To create cardiac tissues of a variable global organization with no significant downstream effect differences from maximally anisotropic tissues, and to determine if a basic force vector addition model [6] could be predictive for the above tissues. As a first step, we formalized the basic model to express the developed stress as a function of tissue organization by making three major simplifications. First simplification: the probability distribution of the sarcomere complex orientations is assumed to be a uniform probability distribution on the interval $[-\theta_0, \theta_0]$ (Fig. S1). This can be written in the following general form:

$$P = \begin{cases} 0 & -\frac{\pi}{2} \le \theta < -\theta_0 \\ \frac{1}{2\theta_0} & -\theta_0 \le \theta \le \theta_0 \\ 0 & \theta_0 < \theta \le \frac{\pi}{2} \end{cases} \quad \text{where} \quad \lim_{\theta_0 \to 0} P = \delta(\theta = 0) \qquad (1)$$

The orientational order parameter (OOP) is a very useful metric to describe construct organization (actin fibrils, sarcomeric z-lines, etc.). The OOP is zero for completely disorganized constructs and one for perfectly organized tissues, and it has been extensively used in many fields [44, 72, 73]. In this case, the OOP is simply a function of the uniform probability interval (θ_0):

$$OOP = \langle \cos(2\theta) \rangle = \int_{-\theta_0}^{\theta_0} \frac{1}{2\theta_0} \cos(2\theta)\, d\theta = \frac{sin(2\theta_0)}{2\theta_0} \qquad (2)$$

Second simplification: the dipole nature of the sarcomere can be ignored; thus, each sarcomere is assumed to produce some average force f_0 in the direction perpendicular to z-lines and parallel to actin fibrils (Fig. 1). Through this assumption, the force vectors became pseudovectors, i.e.

symmetric in π, as the choice of positive or negative direction in a sarcomere complex is random; Thus, the average force produced by a single sarcomere in the *x*-direction is also a function of the uniform probability interval (θ_0):

$$\langle f_x \rangle = \int_{-\theta_0}^{\theta_0} f_0 \cdot \frac{1}{2\theta_0} \cos(\theta)\, d\theta = f_0 \cdot \frac{sin\theta_0}{\theta_0} \tag{3}$$

And, the net force developed by the monolayer is:

$$F = N_{sarcomeres} \cdot \langle f_x \rangle = N_{sarcomeres} \cdot f_0 \cdot \frac{sin\theta_0}{\theta_0} = F_0 \cdot \frac{sin\theta_0}{\theta_0} \tag{4}$$

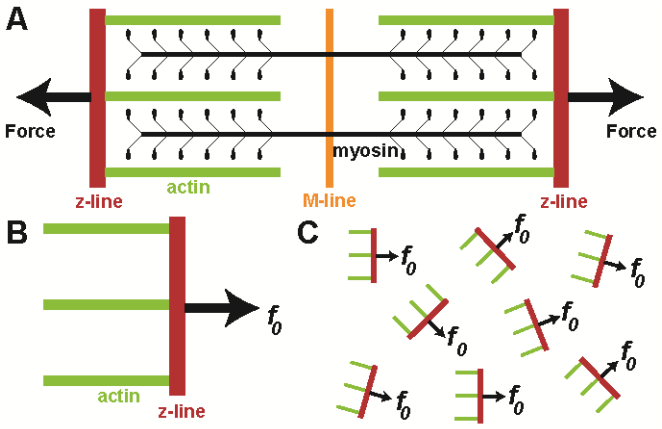

Fig. 1: The basic model approximation of a sarcomere. (A) A sarcomere is a dipole in which force is produced perpendicular to the z-line and parallel to actin fibrils. (B) For the model, the sarcomere is simplified to have a single force vector. (C) Within a cardiac tissue, each sarcomere will produce an average force f_0 parallel to its actin fibrils.

Third simplification: the density of the sarcomeres is the same for all tissue organizations in both the plane and the thickness of the tissue; thus, the stress generated by such a tissue will be proportional to the net force ($\sigma \propto F$) and therefore:

$$\sigma = \sigma_0 \frac{\sin\theta_0}{\theta_0} \tag{5}$$

In this formulation, σ_0 is the stress that would be produced by the tissue if the sarcomeres were perfectly aligned in the x-direction (i.e. $P = \delta(\theta = 0)$). This perfect stress can be calculated as long as both actual stress and organization are known and is the single parameter of this basic model:

$$\sigma_0 = \frac{\sigma}{\left(\frac{sin\theta_0}{\theta_0}\right)} \tag{6}$$

Together, these assumptions can be used to predict the stress as a function of organization (OOP) by solving for θ_0 from equation (2) and inserting the value into equation (5). Equation (5) can be reformulated to predict a stress based on a measurement. For example, the stress produced by an isotropic tissue with no downstream effects can be predicted based on the measured stress of the anisotropic tissue and the organizational information for both tissue types ($\theta_{0,aniso}, \theta_{0,iso}$):

$$\sigma_{iso,predicted} = \sigma_{aniso,measured} \cdot \frac{\sin(\theta_{0,iso}) \cdot \theta_{0,aniso}}{\sin(\theta_{0,aniso}) \cdot \theta_{0,iso}} \quad (7)$$

To properly test even this simple model, it was necessary to create tissues where the only dominant variable was the global tissue organization. The classical isotropic tissues were cultured on fibronectin (FN) that was disorganized both locally (Fig. 2A) and globally (Fig. 2B). We hypothesized that as long as the cells were organized locally, any downstream effects of global disorganization would be muted to the point of being negligible. To achieve this effect, we utilized microcontact printing such that the FN was patterned in 20 μm lines with 5 μm gaps. The locally organized patterns (Fig. 2C-D) were identical to anisotropic patterns (Fig. 2E-F) within each parquet (Fig. 2C, Fig. 2E). The individual parquets (250 μm x 250 μm) had internal line patterns at 0, 45, 90, and 135 degrees. As a result, the global organization of the parquet FN (Fig. 2D) matched isotropic (Fig. 2B).

To test the hypothesis and model, neonatal rat ventricular myocytes (NRVM) were seeded on the patterns (Fig. 2G-J). Qualitatively, the cells followed the parquet patterns, except for small border regions in between the parquet squares (white rectangle in Fig. 2D, Fig. 2J). To compare the tissues quantitatively, the OOP was calculated for the actin fibrils (Table S1). Whether the border regions were taken into account or not, the global organization of the parquet tissues was not statistically significantly different from the isotropic tissues (Fig. 2K; Global). Locally, the internal organization of the parquets matched the anisotropic organization (Fig. 2K; Local).

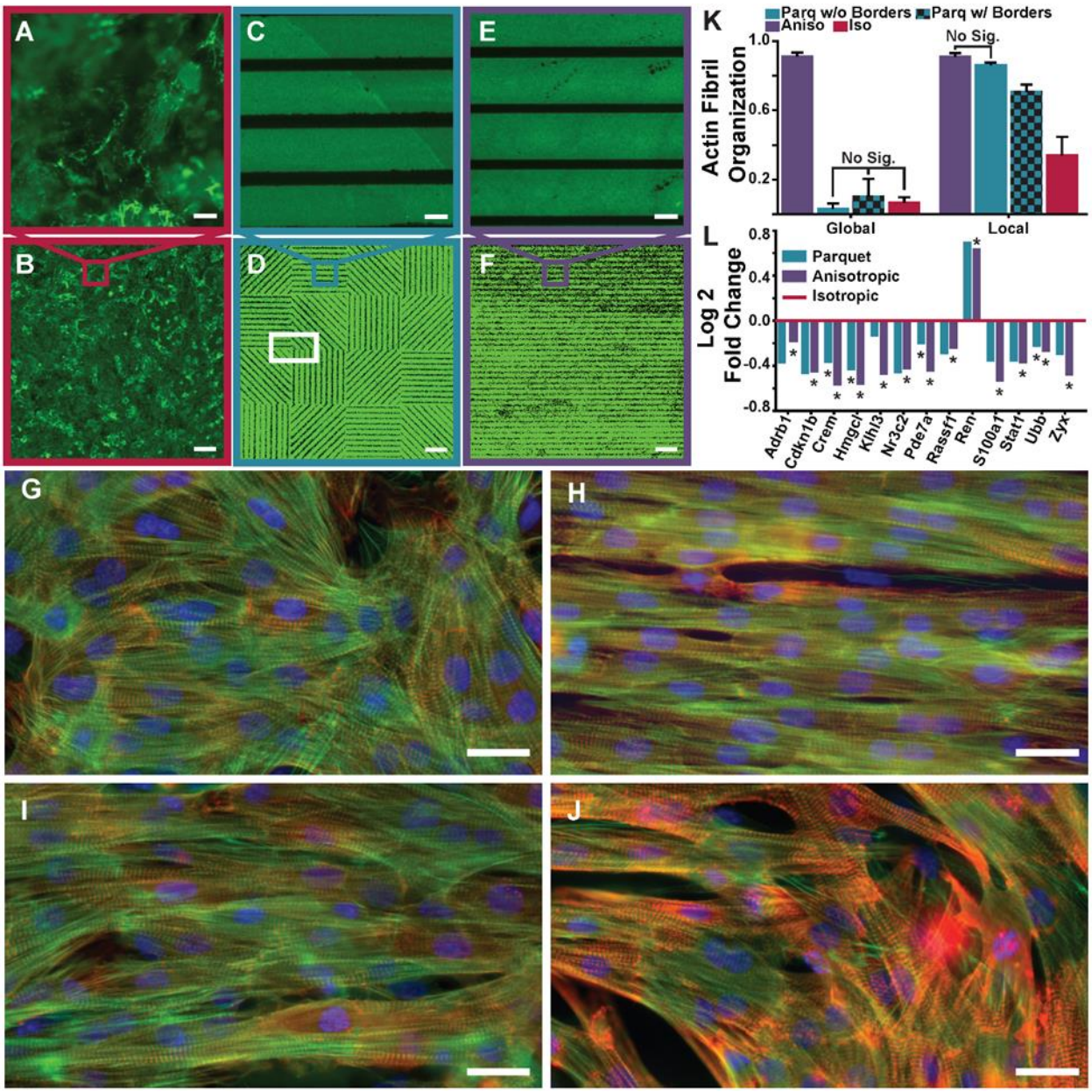

Fig. 2: Locally-organized globally-disorganized parquet tissues. (A & B) Isotropic FN. (C & D) The parquet FN pattern. (E & F) The anisotropic FN pattern. (A,C,E) show the local scale (96 μm x 96 μm) and (B,D,F) show the global scale (1 mm x 1 mm). (G-J) Immunostain images of actin fibrils (green), sarcomeric z-disks (red), and nuclei (blue) for isotropic tissue (G), anisotropic tissue (H), tissues within a parquet tile (I), and tissue from a border region of multiple parquet tiles (J) like the one indicated with the white rectangle in panel D. (K) Actin fibril OOP on the global and local scale for each tissue type. Error bars represent the standard deviation of the data. Significance was tested within each group (global,local), and was $p<0.05$ unless labeled "No. Sig." (Table S1). (L) Log 2 fold change for anisotropic (N=3) and parquet (N=5) samples normalized to isotropic (N=3) samples (Table S2). Scale bars: 10 μm panels A,C,E; 100 μm panels B,D,F; 25 μm panels G-J.

When the border regions were taken into account, the local organization of the parquet tissues was reduced, but still significantly higher than isotropic organization. Next, the parquet tissues were compared to the anisotropic and isotropic tissues by quantifying the gene expression levels, which can be seen as measures of downstream effects.

We tested 84 gene expression levels from a Rat Cardiovascular Disease array (Table S2). There was a statistically significant difference in gene expression between isotropic and anisotropic tissues in 13 genes. Conversely, there was only one gene (Pde7a) whose expression level was significantly different between anisotropic and parquet tissues. However, Pde7a was also among the four genes that were significantly different between parquet and isotropic tissues. Consequently, the gene expression analysis suggested that the parquet tissues tend to be somewhere in between the isotropic and anisotropic tissues (Fig. 2L). These results indicated that we were not able to completely eliminate the downstream effects, but they should have been considerably muted. Therefore, if the proposed highly simplified model encompasses all of the dominant properties of the organization-stress production relationship, the stress measured in the parquet tissues should match the prediction given by equation (7).

To test this, the "heart on a chip" assay [44] was utilized with the three tissue types. In this device, each tissue types was cultured on an elastic polymer film that was partially detached from the glass during contractility experiments. The films were imaged from above and the x-projection was measured for every frame (shown: diastole Fig. 3A and systole Fig. 3B, Videos S1-S3). Samples were paced at 2 hz for consistency, and stress was calculated using previously established procedures [44, 74] (Fig. 3C). The systolic-maximum, diastolic-minimum, and active-amplitude stresses were calculated for each film (Fig. 3D).

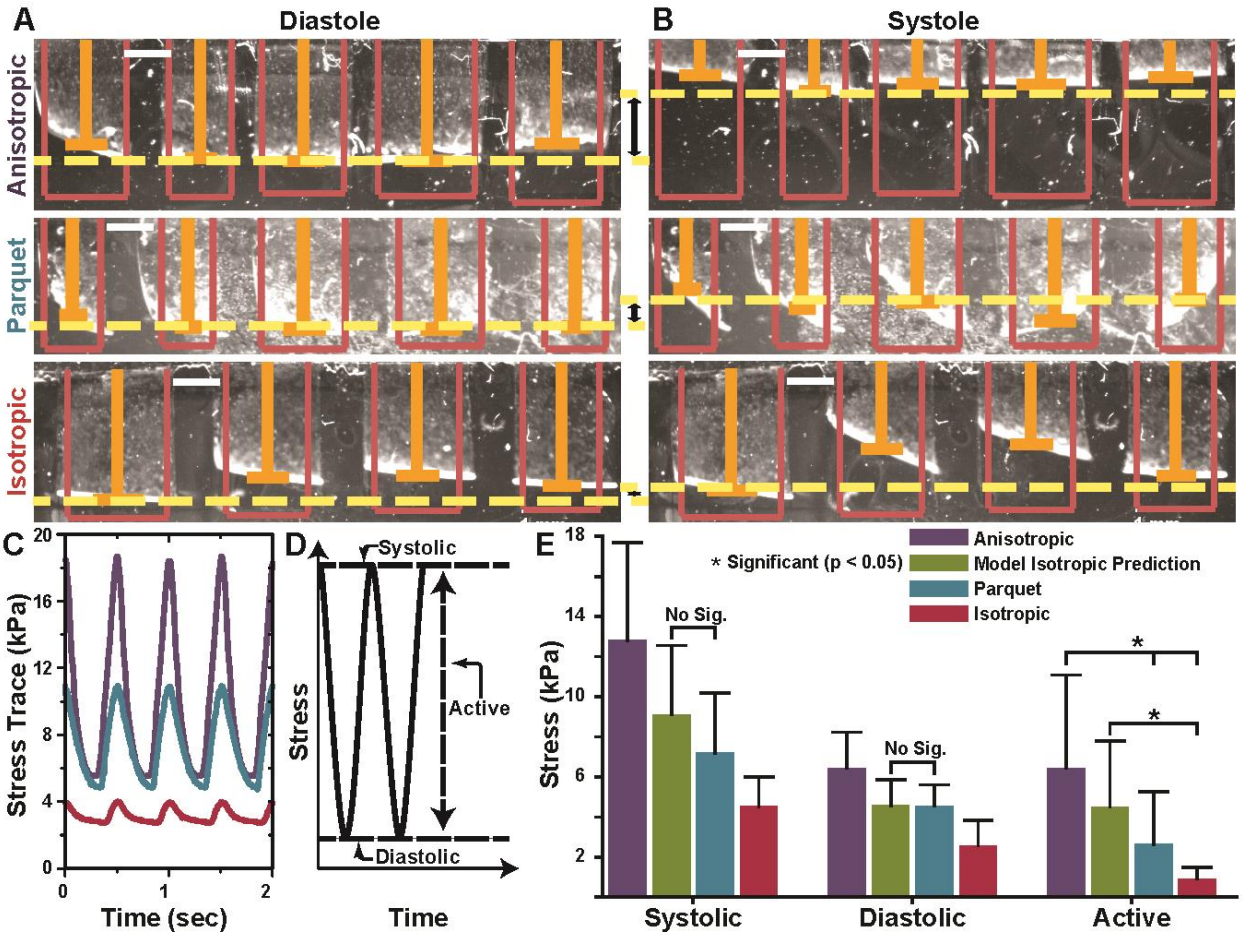

Fig. 3: Contractility experiments using "Heart-on-a-Chip" assays. (A) & (B) Sample video frames for the three tissue types showing diastole and systole, respectively. Pink outlines show original film length, orange bars track films' x-projections, and yellow dashed lines provide a visual cue for the change in contraction between diastole and systole. (Scale bars: 1 mm). (C) Example stress traces of raw data for anisotropic (purple), parquet (blue), and isotropic (red) tissue from a contractility experiment. (D) Schematic of stresses measured from each stress trace. (E) Comparison of stresses for anisotropic (N=28), parquet (N=22), and isotropic (N=27) tissue versus the basic model prediction (green). Significance was assumed if $p<0.05$ (Table S3). Within systolic and diastolic stress, pairwise comparisons were significant unless labeled with "No. Sig." Within Active Stress, pairwise statistical significance is indicated by (*).

To ensure that we did not bias the conclusions in any way, all results were included in the averages unless there was a clear failure to pattern, the cells were not beating in culture, or the chip substrate was defective. This resulted in a significant biological variability, but data from a large enough number of films was collected to test the statistical significance of the findings (Table S3). Using equations (2) and (7), the isotropic stress was predicted based on the measured anisotropic stress and actin fibril organization (Fig. 3E). As expected from previous works, the prediction was statistically different from the measured isotropic stress. However, there was no statistically significant difference between the model prediction and the three types of stresses measured in the parquet tissues. Therefore, these results collectively lead to two interlinked conclusions: The downstream effects were sufficiently muted that they did not significantly affect force production, and more surprisingly, the very basic model encompasses all the dominant features that relate force production to pure tissue organization in engineered monolayer myocyte tissues.

To further test the model and the experimental platform, a range of parquet tissues were created using the tiles depicted in Fig. 4A. The parquet tiles were combined into blocks (Fig. S2) such that the resultant global OOP varied within the isotropic and anisotropic limits (Fig. 4B, Table S4). The average systolic stress for the ideal tissue (Eq. 6) was calculated for each film and averaged to arrive at a single value of σ_0=11.4$\pm$1.2 kPa. Further, the ideal tissue stress was used to predict stress as a function of OOP (Eqs. 2 and 7), and the error was used to derive the 95% confidence limit for the model (Fig. 4C). Hence, the model predicted that the mean of the experimentally measured systolic stress would fall within the interval bound by the 95% confidence limit. Indeed, the mean systolic stress for each parquet pattern was found to be within the 95% confidence limit of the model while the isotropic mean systolic stress was outside the limits (Fig. 4C).

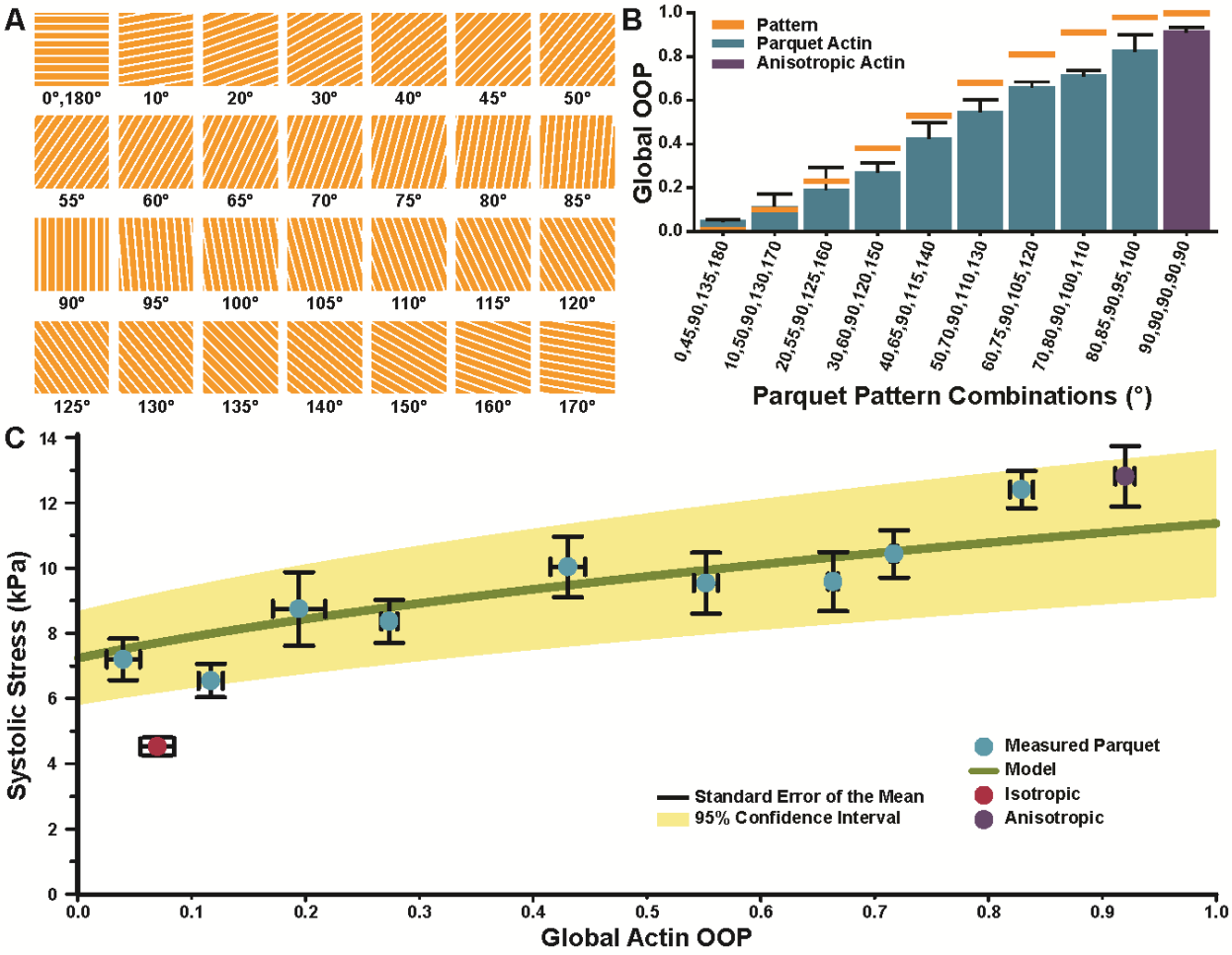

Fig. 4: Experiment vs. model for varying global organization. (A) Various parquet tiles used for tissue design. (B) FN pattern OOP and global actin OOP from all parquet tissues (Table S4). Error bars: Standard deviation. (C) Systolic stress as a function of OOP predicted by the model based on calculated parameter σ_0 (green). The mean systolic stress for each parquet tissue type (blue circles) falls within the 95% confidence limit of the model (light brown). The mean systolic stress of the isotropic tissues (red circle) falls outside the confidence limits of the model. Error bars (black) represent standard error of the mean (Mean$\pm$Standard Deviation for all stresses in Table S5).

Thus, the basic model was found to be predictive for the whole range of organizations as long as the downstream effects were muted and negligible.

Based on this result, it was possible to quantitatively estimate the contribution of the downstream effects to the reduction of stress in isotropic tissues:

$$\sigma_{iso,downstream} = \sigma_{iso,measured} - \sigma_0 \frac{\sin(\theta_{0,iso})}{\theta_{0,iso}} \approx -3.18 \pm 2.61\ kPa \qquad (8)$$

Using the basic model and measured stresses of parquet tissues, it is possible to make this estimate at any organization.

Discussion

In this work, an experimental platform was designed to measure the developed stress as a function of global tissue organization (Fig. 4C). The platform is based on tissues cultured on parquet extracellular matrix patterns, which inside the parquet tiles were identical to the pattern used to make anisotropic tissues (Fig. 2A-K). In the parameter space between classical anisotropic and isotropic tissues, the novel parquet tissues were shown to be in between the two through gene expression levels (Fig. 2L) and similar to anisotropic tissues through local organization (Fig. 2K). This was sufficient to mute the downstream effects associated with isotropic tissues. Indeed, they were negligible as illustrated by the experimental results matching the basic net-force model (Fig. 3E, Fig. 4C). Because of the high biological variability inherent to the contractility measurements (Table S5), it is important to note that the model can only predict mean stresses, not individual film stresses. Thus, if we build a number of tissues with a specified OOP, the model predicts the average systolic stress. Therefore, the new platform can be used to estimate the mean amount of force reduction that can be attributed to downstream effects that might normally be coupled with tissue organization changes.

Common methods of cardiac tissue organization on two-dimensional constructs include microcontact printing, stretch, and topographical cues [6, 8, 11-13]. These methods have been shown to produce anisotropic or isotropic tissues and have been used to study several factors associated with each tissue type [8, 13, 44]. However, in all of these, the reorganization of the tissue also lead to a non-trivial change in functionality. It is possible to create parquet-like organization by providing two perpendicular guidance stimuli like stretch and patterning, but this introduces stretch to the system, which is also known to affect contractility [13]. In contrast, using the parquet tissues made it possible to decouple the global organization from other factors that might have also affected contractile function. Interestingly, the patches of organized tissues are not foreign to the spontaneous self-assembly of isotropic cardiomyocyte monolayers. This was qualitatively evident in small portions of isotropic tissues (Fig. 2G) and emerged quantitatively in that $OOP_{iso,local} > OOP_{iso,global}$ (Fig. 2K). It will take further investigation to determine if the downstream effects are contingent on smaller patches of organization in isotropic compared to parquet tissues or if the local patterning changes the self-assembly cascade, which in turn leads to a difference in the downstream effects. Whatever the causes, our parquet tissue is the simplest method to decouple the global organization from downstream effects that can affect contractility.

Modeling cardiac contractility on the scale of the whole organ [75-77] and at the tissue scale [78, 79] has been extensively pursued. The drastically simplified model presented here could not, and was not meant to, describe all the complexities of the contraction in a cardiac tissue such as the dipole nature of the sarcomeres or the three-dimensional intricate architecture of myofibrils within the heart. Instead, the basic model was designed to work in conjunction with experimental data to provide insight into the causes of changes in force production. However, the discovery that

the relationship between force production and tissue organization is simple when there is no downstream effects will impact the interpretation of model results and design of future models.

It has been shown that variations in cardiac tissue architecture are linked with changes in gene expression [8, 13]. It is not possible to fully understand the effect of these gene expression changes to tissue function without a method by which each can be studied. The proposed platform is a possible remedy to this dilemma. For example, in a comparison study between primary mouse cardiomyocytes and mouse embryonic stem-cell derived cardiomyocyte tissues (ES-tissues), which have very different gene expression profiles, the systolic stresses were found to be approximately 17.1 ± 6.1 kPa and 3.4 ± 1.3 kPa, respectively [58]. However, it is not clear how much of the difference in stress was due to the stem-cell origin of the cells as the tissue organization was also different ($OOP_{primary} \approx 0.71 \pm 0.03$ and $OOP_{stem} \approx 0.35 \pm 0.03$) [58]. Using the method developed here, it is possible to estimate that the primary cells would have produced 9.1 ± 0.9 kPa systolic stress at the ES-tisssue organization. Thus, we can show that -5.7 ± 2.2 kPa of stress difference was due to some factors inherent to the stem-cell derived nature of the ES-tissues. This illustrates the power of our experimental platform and the validated basic model. As more studies are performed on cardiac tissues, our results and the technological platform can be used to explore the functional implications of a variety of biological factors; thus elucidating the mechanisms involved in heart development and disease.

Materials and Methods

Methods are described in detail in the SI Materials and Methods. A brief description is included here.

Substrate Fabrication

For structural and gene-expression studies, 25 mm glass coverslips were cleaned, dried, and coated with Polydimethylsiloxane (PDMS) (Ellsworth Adhesives). Coated coverslips were left to cure overnight in a 60˚C oven. For contractility studies, coverslips were prepared as described by Grosberg et al [44]. Briefly, a large coverglass (Brain Research Laboratories, Newton, MA) was cleaned, dried, and covered with protective film (static cling, Grafix Plastics). The protective film was cut to expose strips of glass onto which poly(N-isopropylacrylamide) (PIPPAm) (Polysciences) was spin-coated. The protective film was removed and the entire coverglass was coated with PDMS and left to cure in a 60˚C oven overnight. Coverglass were cut into individual coverslips using a diamond scriber (Musco Sports Lighting) and a custom template for either 6-well or 12-well culture plates. All substrates were UVO treated before transfer of FN (Jelight).

Extracellular Matrix Patterning

Stamp patterns were designed using Adobe Illustrator software (Adobe Systems Inc.). Designs were etched into 5”x5” chrome with soda-lime glass masks by a third-party vendor (FrontRange Photo Mask Co.). The glass masks were then used to make silicon wafers via SU-8 deposition in the Bio-Organic Nanofabrication Facility (University of California, Irvine), and PDMS stamps were made from the silicon wafer templates.

To microcontact print, we utilized a method similar to that used by Tan et al [5]. Briefly, stamps were cleaned, dried, and evenly coated with 0.1 mg/mL concentration FN (Fisher

Scientific). After a 1 hour incubation, stamps were dried and stamped onto UVO-treated substrates. Blocking was done using pluronics solution (Sigma Aldrich). Isotropic substrates were made by incubating PDMS-coated coverslips with 0.05 mg/mL concentration FN for 10 minutes.

Myocyte harvest, seeding, and culture

All animal protocols were reviewed and approved by the University of California, Irvine, Institutional Animal Care and Use Committee (Protocol No. 2013-3093). Neonatal rat ventricular myocytes (NRVM) were isolated from 2-day old neonatal rats (Charles River Laboratories), enzymatically treated, and dissociated using previously published protocols [6, 44, 80, 81]. Cells were seeded onto prepared substrates at a cell density of 1 million cells per 3 ml.

qPCR

Cells were lysed 72 hours after seeding following RNeasy Mini Kit instructions (Qiagen). Then, cDNA synthesis was accomplished according to the instructions in an RT^2 First Strand Kit (Qiagen). Customized arrays for Rat Cardiovascular Disease were run in triplicate for each sample (PARN-174Z; Qiagen). Data analysis was completed using an online standardized software (Qiagen).

Fixing and Immunostaining

Cells were fixed in warm 4% paraformaldehyde (Fisher Scientific) supplemented with 0.001% Triton X-100 (Sigma Aldrich) and immunostained for actin (A11039; Life Technologies), sarcomeric α-actinin (A7811; Sigma Aldrich), nuclei (D1306; Life Technologies), and FN (F3648; Sigma Aldrich). Secondary staining was done using tetramethylrhodamine- conjugated goat anti-mouse IgG antibody (A21050; Life Technologies) and tetramethylrhodamine- conjugated goat anti-rabbit IgG antibody (A21039; Life Technologies).

Imaging and Image Analysis

Immunostained tissues were imaged on an IX-83 inverted motorized microscope (Olympus) using an UPLFLN 40x oil immersion objective (Olympus). Image processing was done via ImageJ software. Image analysis for orientational order parameter was done using customized MATLAB software as previously described [6, 44]. Cell thicknesses were acquired on an IX-81 Inverted Confocal Microscope (Olympus) using a LUCPLanFLN 40x/0.60 objective (Olympus), and the Fluoview 1200 system (Olympus) (Fig. S3, Table S6).

Contractility Experiments

"Heart-on-a-Chip" experiments were performed 96 hours after seeding in warmed 1X Normal Tyrode's solution according to previously published protocols [44]. Briefly, coverslips were moved out of the incubator, films were cut, and the substrate was lowered to 34˚C to release the films. Samples were paced at 2 hz with 10-12 volts of stimulation. Contractility experiments' movies were acquired on an SZX-ILLB2 Stereoscope (Olympus) inside of an INUL-MS2 Stage Top Incubator (Tokai Hit). Image analysis was completed using a custom ImageJ and MATLAB software as described by Grosberg et al [44].

Statistics

To compare the stress and organization of the anisotropic, parquet, and isotropic tissues, a one way ANOVA with the Holm-Sidak test was used (with overall significance level at 0.05). Gene expression was normalized to isotropic tissue and significance was determined through the online Qiagen software by a Student's t-test between the control group and experimental groups. A p-value of < 0.05 was considered significant and conversely a p-value of > 0.05 was considered non-significant. The confidence interval was calculated using the Confidence function in Excel.

Chapter 2

Supporting Information

Materials and Methods

Substrate Fabrication

For structural and gene-expression studies, round 25 mm glass coverslips were sonicated in 95% ethanol for 30 minutes and incubated in a 60˚C oven for 30 minutes. Polydimethylsiloxane (PDMS) (Ellsworth Adhesives, Germantown, WI) was made using a 1:10 base to curing agent ratio, and the clean coverslips were coated in the PDMS and cured overnight in a 60˚C oven.

For contractility studies, coverslips were prepared as described by Grosberg et al [44]. Briefly, a large coverglass (Brain Research Laboratories, Newton, MA) was sonicated in 50% ethanol for 30 minutes. The coverglass was covered with protective film (static cling) (Grafix Plastics, Cleveland, OH), which was cut and removed using custom templates to provide 1 cm strips of exposed coverglass. Next, 1 gram of poly(N-isopropylacrylamide) (PIPPAm) (Polysciences, Inc., Warrington, PA) was dissolved in 10 mL of 1-butanol (Macron Fine Chemicals, Center Valley, PA). The PIPPAm was then spin-coated onto the exposed coverglass and allowed to dry at room temperature for at least 15 minutes. The remaining static cling was carefully removed from the top and the entire coverglass was coated with the PDMS that had been allowed to cure for five hours. The coverglass was promptly moved to a 60˚C oven to cure overnight. Last, the coverglass was cut into individual coverslips using a diamond scriber (Musco Sports Lighting, LLC. Oskaloosa, IA) and a custom template for either 6-well or 12-well culture plates.

Extracellular Matrix Patterning

Stamp patterns were designed using Adobe Illustrator software (Adobe Systems Inc., San Jose, CA). Stamps were made to be 1.5x1.5 cm to produce fibronectin (FN) lines of 20 μm wide with 5 μm gaps between lines for an anisotropic tissue. Parquet patterns were designed to produce 250x250 μm squares of 20 μm wide lines of FN with 5 μm spacing between lines. Each square had a varying orientation to control the global organization. Patterns started with lines oriented at 0, 45, 90, 135, and 180 degrees to form the locally organized, globally disorganized (isotropic) tissue. Consecutive stamps were designed for each square to be 5 to 10 degrees more oriented towards 90 degrees with the second stamp being 10, 50, 90, 130, and 170 degrees. Eight consecutive stamps were designed with the final parquet stamp being 80, 85, 90, 95, and 100 degrees (Fig. S2).

Designs were etched into 5"x5" chrome with soda-lime glass masks by a third-party vendor (FrontRange Photo Mask Co., Palmer Lake, CO) based on illustrator designs. The glass masks were then used to make silicon wafers via SU-8 deposition in the Bio-Organic Nanofabrication facility (University of California, Irvine). Next, PDMS stamps were made from the silicon wafer templates. To microcontact print, we utilized a method similar to that used by Tan et al [5]. Briefly, the stamps were sonicated in 50% ethanol for 15 minutes and were dried in a biosafety cabinet under sterile conditions using compressed nitrogen. Next, stamps were coated with 0.1 mg/mL concentration FN (Fisher Scientific Company, Hanover Park, IL) and allowed to incubate at room temperature for 1 hour. After the hour incubation, stamps were dried using compressed nitrogen and stamped onto PDMS coated coverslips that had been exposed to UV light (Jelight Company, Inc., Irvine, CA) for 8 minutes. The stamped coverslips were submerged in pluronics solution (5g Pluronics F-127, Sigma Aldrich, Inc., Saint Louis, MO, dissolved in 500 mL sterile water) for 10

minutes and were immediately rinsed three times with room temperature Phosphate Buffered Saline (PBS) (Life Technologies, Carlsbad, CA).

Isotropic tissue samples were made by coating substrates with a uniform layer of FN, allowing the cardiac myocytes to organize randomly (Fig. 2A). Substrates were made by incubating PDMS-coated coverslips, which had been exposed to UV light for 8 minutes, with 300 µL drops of 0.05 mg/mL concentration FN for 10 minutes. The coverslips were then rinsed three time with PBS.

Myocyte harvest, seeding, and culture

Neonatal rat ventricular myocytes (NRVM) were isolated from 2-day old neonatal rats (Charles River Laboratories, Wilmington, MA) [81]. Briefly, ventricular myocardium was excised under sterile conditions in a biosafety cabinet, rinsed in Hanks balanced salt solution buffer (HBSS) (Life Technologies, Carlsbad, CA), and then incubated in a 1 mg/mL trypsin solution (Sigma-Aldrich, Inc., Saint Louis, MO) dissolved in HBSS at 4˚C overnight (12 hours). The trypsin solution was then removed and tissue was neutralized in warmed M199 culture medium (Invitrogen, Carlsbad, CA) supplemented with 10% heat inactivated Fetal Bovine Serum, 10mM HEPES, 20 mM glucose, 2 mM L-glutamine (Life Technologies, Carlsbad, CA), 1.5 µM vitamin B-12 and 50 U/ml penicillin (Sigma-Aldrich Inc., Saint Louis, MO). Media was removed without disturbing tissue and was dissociated through several washes of 1 mg/mL collagenase dissolved in HBSS. Next, collagenase cell solutions were centrifuged at 1200 rpm for 10 minutes. The supernatant was then aspirated and cells were resuspended in chilled HBSS. The HBSS cell solution was then centrifuged again at 1200 rpm for 10 minutes. The supernatant was aspirated and cells were resuspended in warm 10% M199.

The cell solution was purified through three consecutive pre-plates of 45 minutes, 45 minutes, and 40 minutes in cell culture flasks (BD Biosciences, San Diego, CA) in an incubator. After the final preplate, cells were counted using a disposable hemocytometer (Fisher Scientific, Waltham, MA) and were seeded at a density of 1 million cells per 3 ml.

At 24 hours after seeding, dead cells were rinsed from substrates with warmed PBS three times. After washing, warm 10% M199 was added and substrates were returned to the incubator. Then 24 hours later, 10% M199 was replaced with warm 2% M199.

Contractility Experiments

"Heart-on-a-Chip" experiments were performed four days after seeding in warmed 1X Normal Tyrode's solution of 5 mM HEPES (Acros Organics, NJ) ,1 mM Magnesium Chloride (Santa Cruz Biotechnology, Inc., Dallas, TX), 5 mM Glucose, 1.8 mM Calcium Chloride,5.4 mM Potassium Chloride, 135 mM Sodium Chloride, and 0.33 mM Sodium Phosphate (Sigma Aldrich, Inc., Saint Louis, MO). First, patterned substrates were moved into 60 mm petri dishes with warmed 1X Normal Tyrode's solution. Then, substrates were cut into thin films using a razor blade as previously described [44]. The Tyrode's solution and substrates were allowed to cool below 37˚C to dissolve the PIPPAm and release the films from the coverglass surface. Substrates were then moved to a 35 mm petri dish containing 1X Tyrode's solution inside of an INUL-MS2 Stage Top Incubator (Tokai Hit, Fujinomiya-shi, Shizuoka-ken, Japan) to control for temperature. Customized electrodes were affixed to the 35 mm petri dish and films were paced with 10 -12 volts at 2 hz using a MyoPacer Field Stimulator (IonOptix, Milton, MA).

Contractility experiments were acquired on an Olympus SZX-ILLB2 Stereoscope (Olympus America, Center Valley, PA) mounted with a Basler A601f/A602f camera (Basler, Inc., Exton, PA). Short video clips were acquired for each sample and then analyzed using custom

ImageJ and Matlab software (previously described) [44]. Film bending was tracked for each sample and diastole, defined by the longest projection of each film, and systole, defined by the shortest projection of each film, was automatically detected. Each video was labeled with the original length of each film as indicated by a pink outline and film tracking was indicated by an orange bar. Active stress was defined as the difference between systole and diastole for each film (Fig. 3A & B).

Cell and substrate thickness are important parameters in the calculation of muscular thin film contractility [74]. Cell thicknesses for each tissue type were measured, and the average cell thickness for each tissue type was used in thin film analysis. Substrate thickness was measured for each chip using a DektakXT profilometer (Bruker, Tucson, AZ).

Fixing and Immunostaining

Cells were fixed in warm 4% paraformaldehyde (Fisher Scientific Company, Hanover Park, IL) supplemented with 0.001% Triton X-100 (Sigma Aldrich, Inc., Saint Louis, MO) in PBS for 10 minutes. Next, cells were rinsed three times in room temperature PBS for five minutes each wash.

Cells were immunostained for actin (Alex Fluor 488 Phalloidin, Life Technologies, Carlsbad, CA), sarcomeric α-actinin (Mouse Monoclonal Anti-α-actinin, Sigma Aldrich, Inc., Saint Louis, MO), nuclei (4’,6’-diaminodino-2-phenylinodole (DAPI), Life Technologies, Carlsbad, CA), and FN (polyclonal rabbit anti-human fibronectin, Sigma Aldrich, Inc., Saint Louis, MO). Secondary staining was done using tetramethylrhodamine- conjugated goat anti-mouse IgG antibody (Alexa Fluor 633 Goat Anti-Mouse, Life Technologies, Carlsbad, CA) and tetramethylrhodamine- conjugated goat anti-rabbit IgG antibody (Alexa-Fluor 750 Goat Anti-Rabbit, Life Technologies, Carlsbad, CA).

qPCR

Lysate samples were prepared according to the above description. Cells were lysed 72 hours after seeding following RNeasy Mini Kit instructions (Qiagen Inc., Valencia, CA). Lysates were then checked for 260/280 absorbance ratios using a DU 730 UV/Vis spectrophotometer (Beckman Coulter, Brea, CA). Only samples with a ratio between 2.1 and 2.2 were accepted. cDNA synthesis was accomplished according to the instructions in an RT^2 First Strand Kit (Qiagen Inc., Valencia, CA). Customized arrays for Rat Cardiovascular Disease were run in triplicate for each sample (Qiagen Inv., Valencia, CA, Array PARN-174Z). Arrays were run in a CFX96 Real-Time System (Bio-Rad, Irvine, CA). Data analysis was completed using RT^2 Profiler PCR array Data Analysis version 3.5, an online standardized software (Qiagen Inc., Valencia, CA).

Imaging and Image Analysis

Immunostained cells were imaged on an IX-83 inverted motorized microscope (Olympus America, Center Valley, PA) mounted with a digital CCD camera ORCA-R2 C10600-10B (Hamamatsu Photonics, Shizuoka Prefecture, Japan) using an UPLFLN 40x oil immersion objective (Olympus America, Center Valley, PA). At least 10 fields of view were acquired for each sample. Image processing was done via ImageJ software. Image analysis for orientational order parameter was done using customized MATLAB software (MathWorks, Natick, MA) as previously described [6, 44].

Local organization was defined by an area of 215 μm x 164 μm at 40x magnification, an area within the 250 μm x 250 μm squares. Global organization was defined by at least 10 fields of view at 40x magnification, totaling an area of approximately 3.5 mm^2, where the total area of patterned tissue was 225 mm^2 for anisotropic and parquet patterns and 490 mm^2 for isotropic tissues.

Cell thicknesses were acquired on an IX-81 Inverted Olympus Confocal Microscope (Olympus America, Center Valley, PA) mounted with an Edmond Optics EO-4010M camera (Edmond Optics, Barrington, NJ) using a LUCPLanFLN 40x/0.60 objective (Olympus America, Center Valley, PA). Images were acquired using the Fluoview 1200 system with Fluoview Version 4.0 software (Olympus America, Center Valley, PA). At least five fields of view were acquired for each sample and were analyzed as previously described using ImageJ software [6].

Statistics

To compare the stress and organization of the anisotropic, parquet, and isotropic tissues, we used a one way ANOVA with the Holm-Sidak test, which is commonly used for pairwise comparison of experimental groups. Significance was considered for an unadjusted p-value less than the critical level, which accounts for the number of comparisons. This was compared against the Tukey Test to confirm significance outcomes. Gene expression was normalized to isotropic tissue and significance was determined through the online Qiagen software by a Student's t-test between the control group and experimental groups. A p-value of < 0.05 was considered significant and conversely a p-value of > 0.05 was considered non-significant. The confidence interval was calculated using the Confidence function in Excel. The 95% confidence limit indicates that if a sufficient number of samples is collected from the same population, the mean value would be within the limits with a 95% probability.

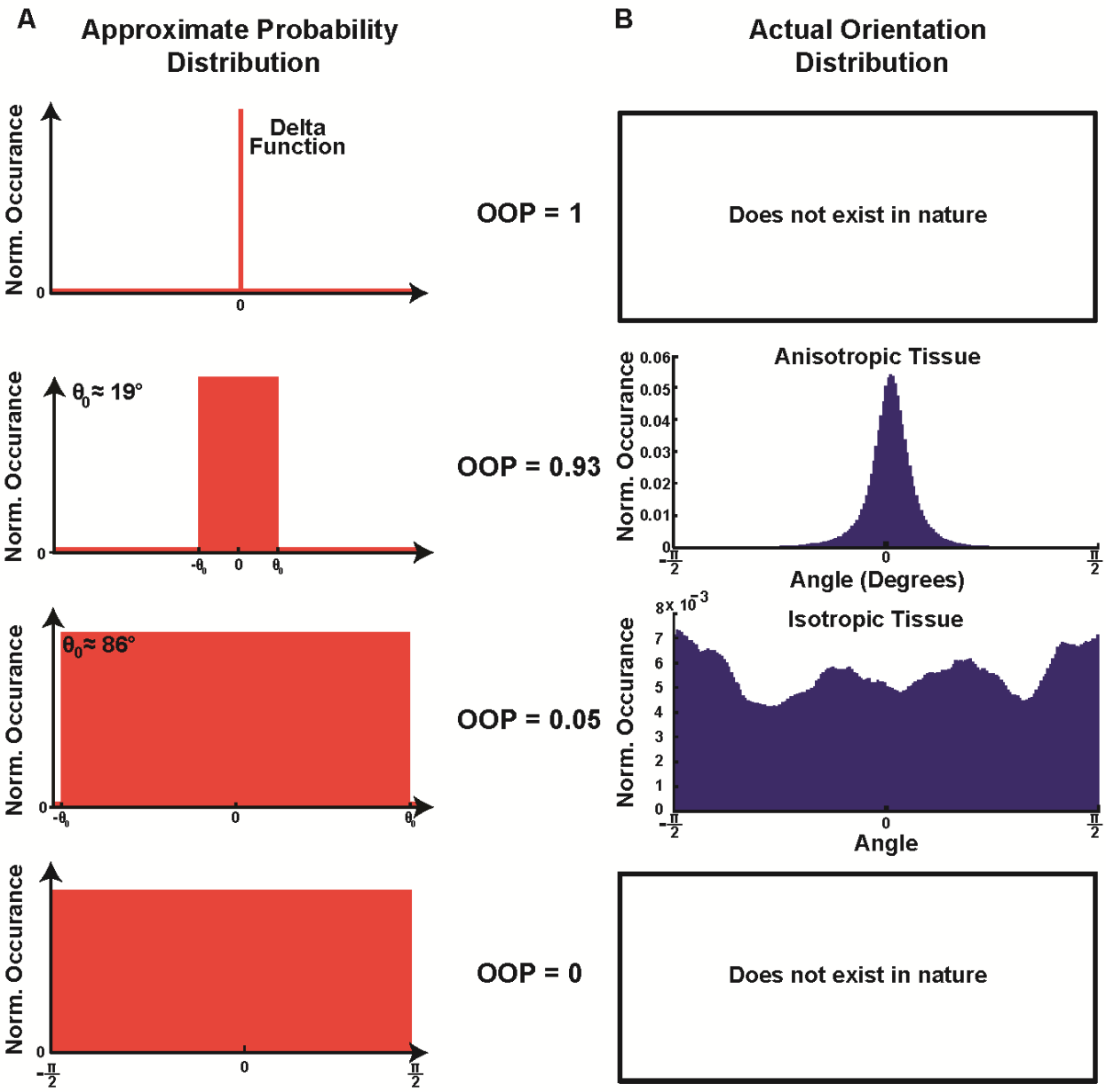

Fig. S1: Approximate probability distribution vs. actual orientation distribution. (A) Analytical representation of the approximate probability distribution of various conditions. An OOP of 1 has a delta function probability distribution. The spread of the probability distribution increases with decreasing OOP until an OOP of 0, at which point the probability is equal for all point on the interval $\left[-\frac{\pi}{2}, \frac{\pi}{2}\right]$. (B) In nature, the constructs do not reach an OOP of 1 or 0, but rather some in between OOP. A well-organized anisotropic tissue can achieve an OOP close to 1 and a disorganized isotropic tissue can reach an OOP value close to 0.

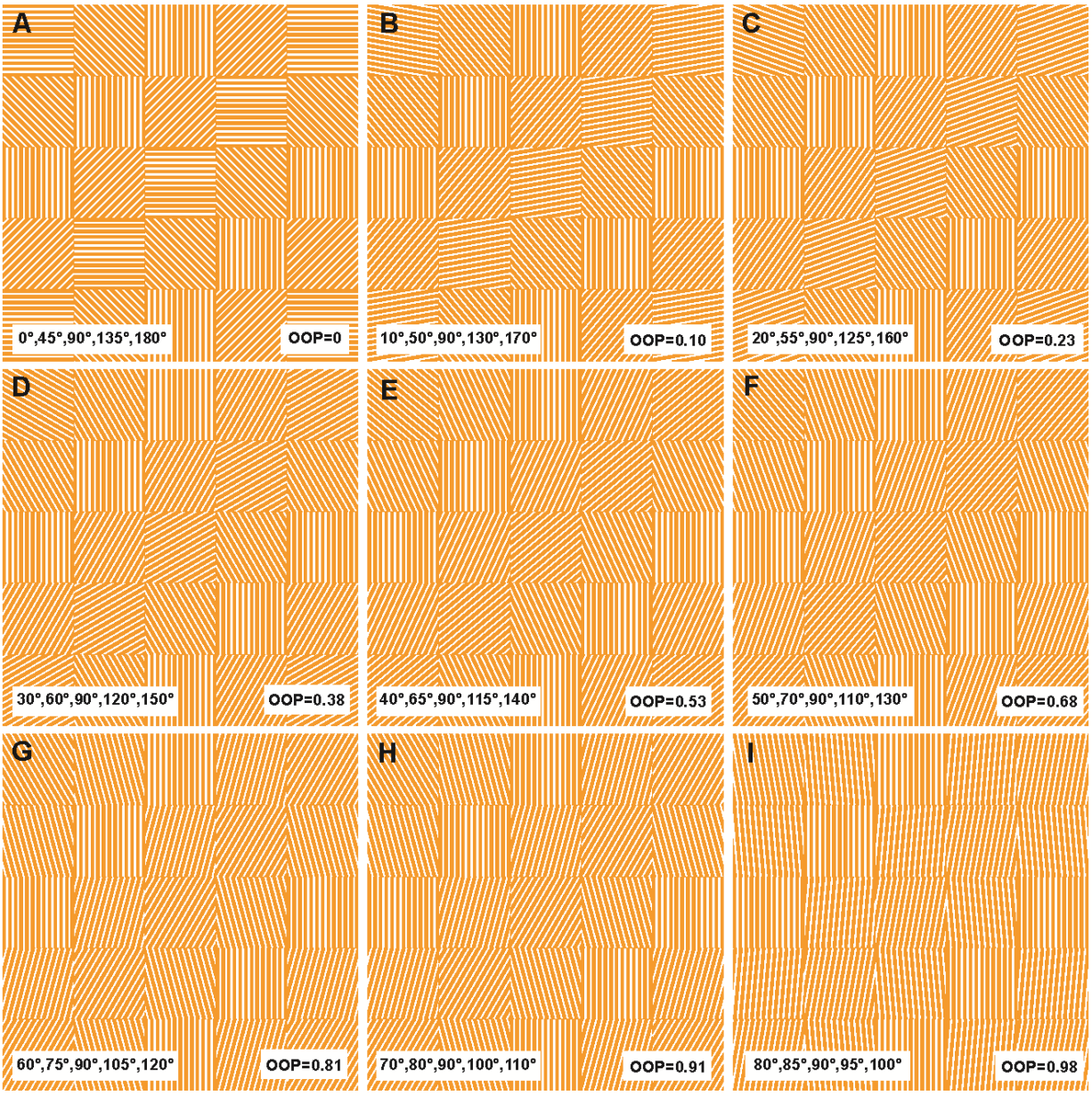

Fig. S2: Parquet patterns. Sample schematic of parquet variations from least organized to most organized (A-I).

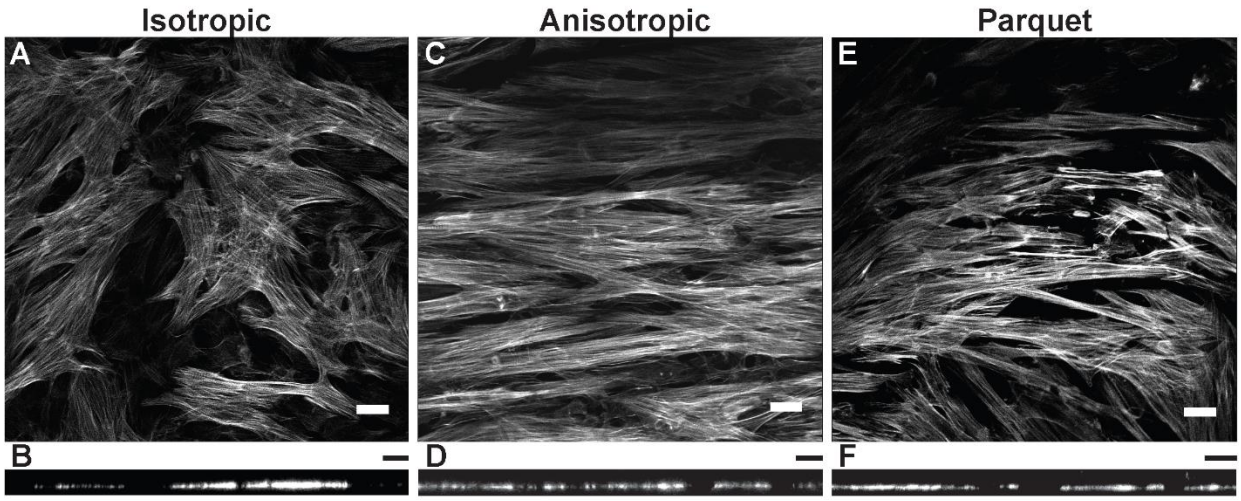

Fig. S3: Confocal images of cell thickness. (A,C,E) Z-stacks were obtained for isotropic (N=4), anisotropic (N=4), and parquet (N=3) samples. (B,D,F) Orthogonal views were used to determine cell thickness (Table S6). Scale bars: 25 µm all panels.

Table S1: List of Local and Global OOP data and statistics for each tissue represented in Fig. 2K. Overall significance level is set to 0.050. (Values are Mean±Standard Deviation).

Tissue Type	Actin Local OOP	Actin Global OOP	Sample Size
Anisotropic	**0.92 ± 0.01**	**0.92 ± 0.01**	**3**
Parquet Images Excluding Borders	**0.88 ± 0.01**	**0.04 ± 0.03**	**3**
Parquet Images Including Borders	**0.81 ± 0.05**	**0.11 ± 0.09**	**3**
Isotropic	**0.45 ± 0.04**	**0.07 ± 0.03**	**3**

Comparison of Global OOP	Unadjusted p-value	Critical Level	Significant?
Anisotropic vs. Parquet w/o borders	**<0.001**	**0.009**	**Yes**
Anisotropic vs. Isotropic	**<0.001**	**0.010**	**Yes**
Anisotropic vs. Parquet w/ borders	**<0.001**	**0.013**	**Yes**
Parquet w/o borders vs. Parquet w/ borders	**0.119**	**0.017**	**No**
Parquet w/o borders vs. Isotropic	**0.405**	**0.025**	**No**
Parquet w/ borders vs. Isotropic	**0.411**	**0.050**	**No**

Comparison of Local OOP	Unadjusted p-value	Critical Level	Significant?
Anisotropic vs. Isotropic	**<0.001**	**0.009**	**Yes**
Parquet w/o borders vs. Isotropic	**<0.001**	**0.010**	**Yes**
Parquet w/ borders vs. Isotropic	**<0.001**	**0.013**	**Yes**
Anisotropic vs. Parquet w/o borders	**0.002**	**0.017**	**Yes**
Parquet w/o borders vs. Parquet w/ borders	**0.008**	**0.025**	**Yes**
Anisotropic vs. Parquet w/ borders	**0.299**	**0.050**	**No**

Table S2: List of genes tested in Rat Cardiovascular Disease Array. Genes in red were significantly different between isotropic and anisotropic tissues. P-values in blue indicate genes for which the expression was undetected and thus the fold-change result was erroneous or un-interpretable as determined by the online software.

Gene Symbol	Description	Function	p-value (compared to anisotropic)	p-value (compared to isotropic)	
			Parquet	Parquet	Anisotropic
Pde7a	Phosphodiesterase 7A	Signal Transduction	0.024	0.034	0.011
Ubb	Ubiquitin B	Apoptosis	0.485	0.011	0.015
Hmgcl	3-hydroxymethyl-3-methylglutaryl-Coenzyme A lyase	Signal Transduction	0.287	0.032	0.047
Crem	CAMP responsive element modulator	Transcriptional Regulation	0.283	0.045	0.002
Zyx	Zyxin	Apoptosis	0.192	0.054	0.042
Nr3c2	Nuclear receptor subfamily 3, group C, member 2	Signal Transduction	0.969	0.064	0.031
Rassf1	Ras association (RalGDS/AF-6) domain family member 1	Signal Transduction	0.785	0.067	0.046
Cdkn1b	Cyclin-dependent kinas inhibitor 1B	Cell Cycle	0.974	0.074	0.050
Adrb1	Adrenergic, beta-1-, receptor	Signal Transduction	0.631	0.086	0.050
Ren	Renin	Cardiac Remodeling	0.697	0.097	0.015
Stat1	Signal transducer and activator of transcription 1	Transcriptional Regulation	0.854	0.118	0.019
S100a1	S100 calcium binding protein A1	Stress & Immune Response	0.487	0.275	0.049
Klhl3	Kelch-like family member 3	Transcriptional Regulation	0.109	0.479	0.015
Actc1	Actin, alpha, cardiac muscle 1	Sarcomere Structural Proteins	0.887	0.068	0.241
Adra1a	Adrenergic, alpha-1A-, receptor	Signal Transduction	0.214	0.262	0.173

Gene Symbol	Description	Function	p-value (compared to anisotropic)	p-value (compared to isotropic)	
			Parquet	Parquet	Anisotropic
Adra1a	Adrenergic, alpha-1A-, receptor	Signal Transduction	0.214	0.262	0.173
Adra1b	Adrenergic, alpha-1B-, receptor	Signal Transduction	0.908	0.568	0.514
Adra1d	Adrenergic, alpha-1D-, receptor	Signal Transduction	0.837	0.193	0.075
Adrb2	Adrenergic, beta-2-, receptor,surface	Signal Transduction	0.754	0.689	0.230
Adrb3	Adrenergic, beta-3-, receptor	Signal Transduction	0.542	0.542	0.217
Aebp1	AE binding protein 1	Cardiac Remodeling	0.855	0.945	0.860
Agtr1a	Angiotensin II receptor, type 1a	Signal Transduction	0.389	0.270	0.081
Anxa4	Annexin A4	Cardiac Remodeling	0.490	0.339	0.177
Ar	Androgen receptor	Signal Transduction	0.995	0.193	0.170
Atp2a2	ATPase, Ca++ transporting, cardiac muscle, slow twitch 2	Transporters	0.780	0.096	0.086
Atp5a1	ATP synthase, H+ transporting, mitochondrial F1 complex, alpha subunit 1, cardiac muscle	Transporters	0.396	0.412	0.934
C6	Complement component 6	Stress & Immune Response	0.475	0.504	0.852
Ccl11	Chemokine (C-C motif) ligand 11	Stress & Immune Response	0.235	0.233	0.184
Ccl2	Chemokine (C-C motif) ligand 2	Stress & Immune Response	0.892	0.870	0.787
Ccnd1	Cyclin D1	Cell Cycle	0.214	0.262	0.173
Col11a1	Collagen, type XI, alpha 1	Cardiac Remodeling	0.908	0.568	0.514

Gene Symbol	Description	Function	p-value (compared to anisotropic)	p-value (compared to isotropic)	
			Parquet	Parquet	Anisotropic
Col1a1	Collagen, type I, alpha 1	Cardiac Remodeling	0.424	0.664	0.294
Col3a1	Collagen, type III, alpha 1	Cardiac Remodeling	0.838	0.619	0.640
Creb5	CAMP responsive element binding protein 5	Transcriptional Regulation	0.068	0.200	0.132
Cryab	Crystallin, alpha B	Sarcomere Structural Proteins	0.487	0.450	0.118
Crym	Crystallin, mu	Sarcomere Structural Proteins	0.581	0.275	0.249
Ctgf	Connective tissue growth factor	Cell Growth	0.735	0.197	0.214
Cxcl12	Chemokine (C-X-C motif) ligand 12 (stromal cell-derived factor 1)	Stress & Immune Response	0.864	0.312	0.270
Dcn	Decorin	Cardiac Remodeling	0.829	0.488	0.373
Dmd	Dystrophin	Cardiac Remodeling	0.943	0.378	0.195
Dusp6	Dual specificity phosphatase 6	Signal Transduction	0.933	0.900	0.949
Enah	Enabled homolog (Drosophila)	Transcriptional Regulation	0.454	0.124	0.185
Epor	Erythropoietin receptor	Signal Transduction	0.481	0.734	0.668
F2r	Coagulation factor II (thrombin) receptor	Cardiac Remodeling	0.256	0.607	0.182
Fn1	Fibronectin 1	Cardiac Remodeling	0.878	0.089	0.051
Frzb	Frizzled-related protein	Signal Transduction	0.732	0.464	0.717
G0s2	G0/G1 switch 2	Cell Cycle	0.739	0.652	0.976
Gja1	Gap junction protein, alpha 1	Cardiac Remodeling	0.385	0.126	0.750

Gene Symbol	Description	Function	p-value (compared to anisotropic)	p-value (compared to isotropic)	
			Parquet	Parquet	Anisotropic
Hmgcr	3-hyroxy-3-methylglutaryl-Coenzyme A reductase	Signal Transduction	0.890	0.053	0.064
Hmgn2	High mobility group nucleosomal binding domain 2	Transcriptional Regulation	0.149	0.796	0.242
Maoa	Monoamine oxidase A	Apoptosis	0.412	0.257	0.591
Mapk1	Mitogen activated protein kinase 1	Signal Transduction	0.746	0.133	0.099
Mapk8	Mitogen activated protein kinase 8	Signal Transduction	0.866	0.509	0.429
Msi2	Musashi RNA-binding protein 2	Transcriptional Regulation	0.775	0.067	0.202
Myh10	Myosin, heavy chain 10, non-muscle	Sarcomere Structural Proteins	0.671	0.357	0.243
Myh6	Myosin, heavy chain 6, cardiac muscle, alpha	Sarcomere Structural Proteins	0.593	0.641	0.975
Ndufb5	NADH dehydrogenase (ubiquinone) 1 beta subcomplex, 5	Apoptosis	0.894	0.205	0.274
Nebl	Nebulette	Sarcomere Structural Proteins	0.917	0.263	0.352
Nfia	Nuclear factor I/A	Transcriptional Regulation	0.667	0.627	0.453
Nkx2-5	NK2 transcription factor related, locus 5 (dDrosophila)	Transcriptional Regulation	0.115	0.092	0.069
Nppa	Natriuretic peptide precursor A	Apoptosis	0.222	0.136	0.126
Nppb	Natriuretic peptide precursor B	Apoptosis	0.347	0.307	0.260
Npr1	Natriuretic peptide receptor A/guanylate cyclase A (atrionatriuretic peptide receptor A)	Apoptosis	0.958	0.321	0.123

Gene Symbol	Description	Function	p-value (compared to anisotropic)	p-value (compared to isotropic)	
			Parquet	Parquet	Anisotropic
Npr2	Natriuretic peptide receptor B/guanylate cyclase (atrionatriuretic peptide receptor B)	Signal Transduction	0.643	0.187	0.051
Npr3	Natriuretic peptide receptor A/guanylate cyclase C (atrionatriuretic peptide receptor C)	Signal Transduction	0.879	0.799	0.652
Nr3c1	Nuclear receptor subfamily 3, group C, member 1	Signal Transduction	0.655	0.071	0.161
Pde3a	Phosphodiesterase 3A, cGMP inhibited	Apoptosis	0.964	0.166	0.199
Pde3b	Phosphodiesterase 3B, cGMP inhibited	Signal Transduction	0.642	0.119	0.211
Pde5a	Phosphodiesterase 5A, cGMP inhibited	Signal Transduction	0.625	0.237	0.481
Postn	Periostin, osteoblast specific factor	Sarcomere Structural Proteins	0.239	0.897	0.328
Ptn	Pleiotrophin	Cell Growth	0.820	0.846	0.939
Rarres1	Retinoic acid receptor responder (tazarotene induced) 1	Cell Cycle	0.807	0.999	0.419
Rtn4	Reticulon 4	Cardiac Remodeling	0.436	0.060	0.110
S100a8	S100 calcium binding protein A8	Stress & Immune Response	0.794	0.718	0.863
Serpina3n	Serin (or cysteine) peptidase inhibitor, clase A, member 3N	Cardiac Remodeling	0.837	0.950	0.756
Sfrp4	Secreted frizzled-related protein 4	Cell Growth	0.445	0.731	0.387
Snca	Synuclein, alpha (non A4 component of amyloid precursor)	Apoptosis	0.828	0.531	0.534
Spock1	Sparc/osteonectin, cwcv and kazal-like domains proteoglycan (testican) 1	Cell Growth	0.768	0.954	0.594

Gene Symbol	Description	Function	p-value (compared to anisotropic)	p-value (compared to isotropic)	
			Parquet	Parquet	Anisotropic
Tcf4	Transcription factor 4	Transcriptional Regulation	0.698	0.137	0.089
Thbs2	Thrombospondin 2	Apoptosis	0.964	0.917	0.963
Tnni3	Troponin I type 3 (cardiac)	Cardiac Remodeling	0.837	0.219	0.125
Tnnt2	Troponin T type 2 (cardiac)	Cardiac Remodeling	0.604	0.159	0.144
Ace	Angiotensin I converting enzyme (peptidyl-dipeptidase A) 1	Cell Growth	0.700	0.288	0.015
Mmp13	Matrix metallopeptidase 13	Cardiac Remodeling	0.700	0.288	0.015
Slc12a1	Solute carrier family 12 (sodium/potassium/chloride transporters), member 1	Signal Transduction	0.700	0.288	0.015

Table S3: List of experimental data and statistics for all tissue types for each respective stress as represented in Fig. 3D. Overall significance level is set to 0.050. (Values are Mean±Standard Deviation).

Tissue Type	Systolic Stress (kPa)	Diastolic Stress (kPa)	Active Stress (kPa)	Sample Size
Anisotropic	**12.8 ± 4.87**	**6.46 ± 1.78**	**6.36 ± 4.63**	**28**
Model	**9.10 ±3.46**	**4.58 ± 1.26**	**4.51 ± 3.29**	**22**
Parquet	**7.20 ± 2.99**	**4.56 ± 1.04**	**2.64 ± 2.63**	**28**
Isotropic	**4.53 ± 1.46**	**2.56 ± 1.27**	**0.91 ± 0.59**	**27**

Comparison of Systolic Stress	Unadjusted p-value	Critical Level	Significant?
Anisotropic vs. Isotropic	**<0.001**	**0.009**	**Yes**
Anisotropic vs. Parquet	**<0.001**	**0.010**	**Yes**
Model vs. Isotropic	**<0.001**	**0.013**	**Yes**
Anisotropic vs. Model	**<0.001**	**0.017**	**Yes**
Parquet vs. Isotropic	**0.008**	**0.025**	**Yes**
Model vs. Parquet	**0.057**	**0.050**	**No**

Comparison of Diastolic Stress	Unadjusted p-value	Critical Level	Significant?
Anisotropic vs. Isotropic	**<0.001**	**0.009**	**Yes**
Model vs. Isotropic	**<0.001**	**0.010**	**Yes**
Anisotropic vs. Model	**<0.001**	**0.013**	**Yes**
Parquet vs. Isotropic	**<0.001**	**0.017**	**Yes**
Anisotropic vs. Parquet	**<0.001**	**0.025**	**Yes**
Model vs. Parquet	**0.953**	**0.050**	**No**

Comparison of Active Stress	Unadjusted p-value	Critical Level	Significant?
Anisotropic vs. Isotropic	**<0.001**	**0.009**	**Yes**
Model vs. Isotropic	**<0.001**	**0.010**	**Yes**
Anisotropic vs. Parquet	**<0.001**	**0.013**	**Yes**
Anisotropic vs. Model	**0.033**	**0.017**	**No**
Model vs. Parquet	**0.041**	**0.025**	**No**
Parquet vs. Isotropic	**0.061**	**0.050**	**No**

Table S4: List of experimental actin OOP values for each tissue type including number of samples. (Values are Mean±Standard Deviation).

Tissue Type	Pattern OOP	Actin Global OOP	No. of Chips
Isotropic	**0.00**	**0.09 ± 0.03**	**3**
Parquet (0,45,90,135,180)	**0.00**	**0.05 ± 0.00**	**3**
Parquet (10,50,90,130,170)	**0.10**	**0.12 ± 0.05**	**6**
Parquet (20,55,90,125,160)	**0.23**	**0.19 ± 0.10**	**5**
Parquet (30,60,90,120,150)	**0.38**	**0.27 ± 0.04**	**6**
Parquet (40,65,90,115,140)	**0.53**	**0.43 ± 0.07**	**4**
Parquet (50,70,90,110,130)	**0.68**	**0.55 ± 0.05**	**4**
Parquet (60,75,90,105,120)	**0.81**	**0.66 ± 0.02**	**3**
Parquet (70,80,90,100,110)	**0.91**	**0.72 ± 0.02**	**9**
Parquet (80,85,90,95,100)	**0.98**	**0.83 ± 0.07**	**8**
Anisotropic = (90,90,90,90,90)	**1.00**	**0.92 ± 0.01**	**3**

Table S5: List of experimental sample sizes for each tissue type including average measured systolic stress, number of samples, number of chips, and number of harvests across which each pattern was tests. Error represented as standard deviation.

Tissue Type	Average Systolic Stress (kPa)	No. of Samples	No. of Chips	Across No. of Harvests
Isotropic	**4.53 ± 1.46**	**27**	**8**	**3**
Parquet (0,45,90,135,180)	**7.20 ± 2.99**	**22**	**6**	**2**
Parquet (10,50,90,130,170)	**6.55 ± 2.62**	**26**	**6**	**4**
Parquet (20,55,90,125,160)	**8.75 ± 4.92**	**19**	**5**	**3**
Parquet (30,60,90,120,150)	**8.73 ± 3.62**	**30**	**6**	**5**
Parquet (40,65,90,115,140)	**10.0 ± 4.16**	**20**	**4**	**3**
Parquet (50,70,90,110,130)	**9.54 ± 4.37**	**22**	**4**	**3**
Parquet (60,75,90,105,120)	**9.59 ± 4.45**	**24**	**4**	**3**
Parquet (70,80,90,100,110)	**10.4 ± 5.43**	**56**	**9**	**3**
Parquet (80,85,90,95,100)	**12.4 ± 4.01**	**50**	**8**	**3**
Anisotropic = (90,90,90,90,90)	**12.8 ± 4.87**	**28**	**7**	**3**

Table S6: List of tissue thicknesses measured for each tissue type with corresponding samples sizes. Error represented as standard deviation.

Tissue Type	Measured Cell Thickness (μm)	No. of Samples
Anisotropic	**4.9 ± 0.9**	**4**
Isotropic	**6.6 ± 1.4**	**4**
Parquet (0,45,90,135,180)	**5.4 ± 0.5**	**3**

References

[1] F. Ahmad, J. G. Seidman, and C. E. Seidman, "The genetic basis for cardiac remodeling," in *Annual Review of Genomics and Human Genetics*. vol. 6, ed Palo Alto: Annual Reviews, 2005, pp. 185-216.

[2] C. Ho, "Hypertrophic Cardiomyopathy: Preclinical and Early Phenotype," *Journal of Cardiovascular Translational Research,* vol. 2, pp. 462-470, 2009/12/01 2009.

[3] P. A. Helm, L. Younes, M. F. Beg, D. B. Ennis, C. Leclercq, O. P. Faris, E. McVeigh, D. Kass, M. I. Miller, and R. L. Winslow, "Evidence of structural remodeling in the dyssynchronous failing heart," *Circ Res,* vol. 98, pp. 125-32, Jan 6 2006.

[4] T. Matsushita, M. Oyamada, K. Fujimoto, Y. Yasuda, S. Masuda, Y. Wada, T. Oka, and T. Takamatsu, "Remodeling of cell-cell and cell-extracellular matrix interactions at the border zone of rat myocardial infarcts," *Circ Res,* vol. 85, pp. 1046-55, 1999.

[5] J. L. Tan, W. Liu, C. M. Nelson, S. Raghavan, and C. S. Chen, "Simple approach to micropattern cells on common culture substrates by tuning substrate wettability," *Tissue Eng,* vol. 10, pp. 865-72, 2004.

[6] A. W. Feinberg, P. W. Alford, H. Jin, C. M. Ripplinger, A. A. Werdich, S. P. Sheehy, A. Grosberg, and K. K. Parker, "Controlling the contractile strength of engineered cardiac muscle by hierarchal tissue architecture," *Biomaterials,* vol. 33, pp. 5732-41, Aug 2012.

[7] D. H. Kim, E. A. Lipke, P. Kim, R. Cheong, S. Thompson, M. Delannoy, K. Y. Suh, L. Tung, and A. Levchenko, "Nanoscale cues regulate the structure and function of macroscopic cardiac tissue constructs," *Proc Natl Acad Sci U S A,* vol. 107, pp. 565-70, Jan 12 2010.

[8] C. Y. Chung, H. Bien, E. A. Sobie, V. Dasari, D. McKinnon, B. Rosati, and E. Entcheva, "Hypertrophic phenotype in cardiac cell assemblies solely by structural cues and ensuing self-organization," *FASEB J,* vol. 25, pp. 851-62, Mar 2011.

[9] A. Agarwal, Y. Farouz, A. P. Nesmith, L. F. Deravi, M. L. McCain, and K. K. Parker, "Micropatterning Alginate Substrates for In Vitro Cardiovascular Muscle on a Chip," *Advanced Functional Materials,* pp. n/a-n/a, 2013.

[10] M. L. McCain, A. Agarwal, H. W. Nesmith, A. P. Nesmith, and K. K. Parker, "Micromolded gelatin hydrogels for extended culture of engineered cardiac tissues," *Biomaterials,* vol. 35, pp. 5462-71, 2014.

[11] A. Chen, D. K. Lieu, L. Freschauf, V. Lew, H. Sharma, J. Wang, D. Nguyen, I. Karakikes, R. J. Hajjar, A. Gopinathan, E. Botvinick, C. C. Fowlkes, R. A. Li, and M. Khine, "Shrink-Film Configurable Multiscale Wrinkles for Functional Alignment of Human Embryonic Stem Cells and their Cardiac Derivatives," *Advanced Materials,* vol. 23, pp. 5785-5791, 2011.

[12] T. Matsuda, K. Takahashi, T. Nariai, T. Ito, T. Takatani, Y. Fujio, and J. Azuma, "N-cadherin-mediated cell adhesion determines the plasticity for cell alignment in response to mechanical stretch in cultured cardiomyocytes," *Biochem Biophys Res Commun,* vol. 326, pp. 228-232, 2004.

[13] M. L. McCain, S. Sheehy, A. Grosberg, J. A. Goss, and K. K. Parker, "Recapitulating maladaptive, mulitscale remodeling of failing myocardium on a chip," *PNAS,* vol. 110, p. 6, 2013.

[14] O. Caspi, A. Lesman, Y. Basevitch, A. Gepstein, G. Arbel, I. Habib, L. Gepstein, and S. Levenberg, "Tissue engineering of vascularized cardiac muscle from human embryonic stem cells," *Circ Res,* vol. 100, p. 10, 2007 Feb 2 2007.
[15] M. R. Badrossamay, K. Balachandran, A. K. Capulli, H. M. Golecki, A. Agarwal, J. A. Goss, H. Kim, K. Shin, and K. K. Parker, "Engineering hybrid polymer-protein super-aligned nanofibers via rotary jet spinning," *Biomaterials,* vol. 35, pp. 3188-3197, 2014.
[16] M. Radisic, H. Park, H. Shing, T. Consi, F. J. Schoen, R. Langer, L. E. Freed, and G. Vunjak-Novakovic, "Functional assembly of engineered myocardium by electrical stimulation of cardiac myocytes cultured on scaffolds," *Proc Natl Acad Sci U S A,* vol. 101, pp. 18129-34, 2004.
[17] M. Radisic, A. Marsano, R. Maidhof, Y. Wang, and G. Vunjak-Novakovic, "Cardiac tissue engineering using perfusion bioreactor systems," *Nat Protoc,* vol. 3, pp. 719-38, 2008.
[18] H. C. Ott, T. S. Matthiesen, S.-K. Goh, L. D. Black, S. M. Kren, T. I. Netoff, and D. A. Taylor, "Perfusion-decellularized matrix: using nature's platform to engineer a bioartificial heart," *Nat Med,* vol. 14, p. 9, 02/2008 2008.
[19] T. Y. Lu, B. Lin, J. Kim, M. Sullivan, K. Tobita, G. Salama, and L. Yang, "Repopulation of decellularized mouse heart with human induced pluripotent stem cell-derived cardiovascular progenitor cells," *Nat Commun,* vol. 4, 2013.
[20] J. J. Feher, *Quantitative Human Physiology: An Introduction*: Elsevier/Academic Press, 2012.
[21] J. J. E. Hall and A. C. Guyton, *Guyton and Hall Textbook of Medical Physiology*: Saunders/Elsevier, 2000.
[22] P. J. Zimetbaum and M. E. Josephson, "Use of the Electrocardiogram in Acute Myocardial Infarction," *New England Journal of Medicine,* vol. 348, pp. 933-940, 2003.
[23] P. A. Carey, M. Turner, C. H. Fry, and D. J. Sheridan, "Reduced Anisotropy of Action Potential Conduction in Left Ventricular Hypertrophy," *Journal of Cardiovascular Electrophysiology,* vol. 12, pp. 830-835, 2001.
[24] M. Antz, K. Otomo, M. Arruda, B. J. Scherlag, J. Pitha, C. Tondo, R. Lazzara, and W. M. Jackman, "Electrical conduction between the right atrium and the left atrium via the musculature of the coronary sinus," *Circulation,* vol. 98, pp. 1790-5, 1998.
[25] I. R. Efimov, V. P. Nikolski, and G. Salama, "Optical imaging of the heart," *Circ Res,* vol. 95, pp. 21-33, 2004.
[26] W. J. Hucker, V. P. Nikolski, and I. R. Efimov, "Optical mapping of the atrioventricular junction," *Journal of Electrocardiology,* vol. 38, pp. 121-125, 2005.
[27] G. E. Morley, D. Vaidya, F. H. Samie, C. Lo, M. Delmar, and J. Jalife, "Characterization of Conduction in the Ventricles of Normal and Heterozygous Cx43 Knockout Mice Using Optical Mapping," *Journal of Cardiovascular Electrophysiology,* vol. 10, pp. 1361-1375, 1999.
[28] N. Bursac, "Cardiomyocyte Cultures With Controlled Macroscopic Anisotropy: A Model for Functional Electrophysiological Studies of Cardiac Muscle," *Circulation Research,* vol. 91, pp. 45e-54, 2002.
[29] V. G. Fast and A. G. Kleber, "Microscopic conduction in cultured strands of neonatal rat heart cells measured with voltage-sensitive dyes," *Circ Res,* vol. 73, pp. 914-25, 1993.

[30] O. Sirenko, C. Crittenden, N. Callamaras, J. Hesley, Y. W. Chen, C. Funes, I. Rusyn, B. Anson, and E. F. Cromwell, "Multiparameter in vitro assessment of compound effects on cardiomyocyte physiology using iPSC cells," *J Biomol Screen,* vol. 18, pp. 39-53, 2013.

[31] V. G. Fast, B. J. Darrow, J. E. Saffitz, and A. G. Kleber, "Anisotropic activation spread in heart cell monolayers assessed by high-resolution optical mapping. Role of tissue discontinuities," *Circ Res,* vol. 79, pp. 115-27, 1996.

[32] N. Bursac, F. Aguel, and L. Tung, "Multiarm spirals in a two-dimensional cardiac substrate," *Proc Natl Acad Sci U S A,* vol. 101, pp. 15530-4, Oct 26 2004.

[33] M. S. Spach, J. F. Heidlage, R. C. Barr, and P. C. Dolber, "Cell size and communication: Role in structural and electrical development and remodeling of the heart," *Heart Rhythm,* vol. 1, pp. 500-515, 2004.

[34] J. D. Humphrey, *Cardiovascular Solid Mechanics: Cells, Tissues, and Organs*: Springer, 2010.

[35] F. J. T. Wackers, H. J. Berger, D. E. Johnstone, L. Goldman, L. A. Reduto, R. A. Langou, A. Gottschalk, B. L. Zaret, L. Quartararo, and L. Pytlik, "Multiple gated cardiac blood pool imaging for left ventricular ejection fraction: Validation of the technique and assessment of variability," *Am J Cardiol,* vol. 43, pp. 1159-1166, 1979.

[36] J. Chen, W. Liu, H. Zhang, L. Lacy, X. Yang, S.-K. Song, S. A. Wickline, and X. Yu, "Regional ventricular wall thickening reflects changes in cardiac fiber and sheet structure during contraction: quantification with diffusion tensor MRI," *American Journal of Physiology - Heart and Circulatory Physiology,* vol. 289, pp. H1898-H1907, 2005-10-11 15:48:08 2005.

[37] B. J. Feild, W. A. Baxley, R. O. Russell, Jr., W. P. Hood, Jr., J. H. Holt, J. T. Dowling, and C. E. Rackley, "Left ventricular function and hypertrophy in cardiomyopathy with depressed ejection fraction," *Circulation,* vol. 47, pp. 1022-31, 1973.

[38] S. N. Mirica, V. Ordodi, A. Apostol, D. Ana, A. Răducan, O. Duicu, M. Hâncu, V. Ivan, and D. Muntean, "Langendorff perfused heart - The 110 years old experimental model that gets better with age," *Studia Universitatis Vasile Goldis Seria Stiintele Vietii (Life Sciences Series),* vol. 19, pp. 81-86, 2009.

[39] T. Boudou, W. R. Legant, A. Mu, M. A. Borochin, N. Thavandiran, M. Radisic, P. W. Zandstra, J. A. Epstein, K. B. Margulies, and C. S. Chen, "A microfabricated platform to measure and manipulate the mechanics of engineered cardiac microtissues," *Tissue Eng Part A,* vol. 18, pp. 910-9, 2012.

[40] N. Thavandiran, N. Dubois, A. Mikryukov, S. Masse, B. Beca, C. A. Simmons, V. S. Deshpande, J. P. McGarry, C. S. Chen, K. Nanthakumar, G. M. Keller, M. Radisic, and P. W. Zandstra, "Design and formulation of functional pluripotent stem cell-derived cardiac microtissues," *Proc Natl Acad Sci U S A,* vol. 110, p. 19, 2013.

[41] A. C. van Spreeuwel, N. A. Bax, A. J. Bastiaens, J. Foolen, S. Loerakker, M. Borochin, D. W. van der Schaft, C. S. Chen, F. P. Baaijens, and C. V. Bouten, "The influence of matrix (an)isotropy on cardiomyocyte contraction in engineered cardiac microtissues," *Integr Biol,* vol. 6, pp. 422-9, 2014.

[42] A. W. Feinberg, A. Feigel, S. S. Shevkoplyas, S. Sheehy, G. M. Whitesides, and K. K. Parker, "Muscular thin films for building actuators and powering devices," *Science,* vol. 317, pp. 1366-70, Sep 7 2007.

[43] A. Grosberg, P. L. Kuo, C. L. Guo, N. A. Geisse, M. A. Bray, W. J. Adams, S. P. Sheehy, and K. K. Parker, "Self-organization of muscle cell structure and function," *PLoS Comput Biol,* vol. 7, p. e1001088, Feb 2011.
[44] A. Grosberg, P. W. Alford, M. L. McCain, and K. K. Parker, "Ensembles of engineered cardiac tissues for physiological and pharmacological study: heart on a chip," *Lab Chip,* vol. 11, pp. 4165-73, Dec 21 2011.
[45] A. Agarwal, J. A. Goss, A. Cho, M. L. McCain, and K. K. Parker, "Microfluidic heart on a chip for higher throughput pharmacological studies," *Lab Chip,* Jun 27 2013.
[46] N. Fausto, "Liver regeneration and repair: Hepatocytes, progenitor cells, and stem cells," *Hepatology,* vol. 39, pp. 1477-1487, 2004.
[47] H. Yin, F. Price, and M. A. Rudnicki, "Satellite cells and the muscle stem cell niche," *Physiol Rev,* vol. 93, pp. 23-67, 2013.
[48] M. Mollova, K. Bersell, S. Walsh, J. Savla, L. T. Das, S. Y. Park, L. E. Silberstein, C. G. Dos Remedios, D. Graham, S. Colan, and B. Kuhn, "Cardiomyocyte proliferation contributes to heart growth in young humans," *Proc Natl Acad Sci U S A,* vol. 110, pp. 1446-51, 2013.
[49] P. Anversa, J. Kajstura, A. Leri, and R. Bolli, "Life and death of cardiac stem cells: a paradigm shift in cardiac biology," *Circulation,* vol. 113, pp. 1451-63, 2006.
[50] L. C. Amado, A. P. Saliaris, K. H. Schuleri, M. St. John, J.-S. Xie, S. Cattaneo, D. J. Durand, T. Fitton, J. Q. Kuang, G. Stewart, S. Lehrke, W. W. Baumgartner, B. J. Martin, A. W. Heldman, and J. M. Hare, "Cardiac repair with intramyocardial injection of allogeneic mesenchymal stem cells after myocardial infarction," *Proc Natl Acad Sci U S A,* vol. 102, pp. 11474-11479, August 9, 2005 2005.
[51] T. E. Robey, M. K. Saiget, H. Reinecke, and C. E. Murry, "Systems approaches to preventing transplanted cell death in cardiac repair," *J Mol Cell Cardiol,* vol. 45, pp. 567-581, 2008.
[52] C. Herberts, M. Kwa, and H. Hermsen, "Risk factors in the development of stem cell therapy," *Journal of Translational Medicine,* vol. 9, p. 29, 2011.
[53] J. J. Chong, X. Yang, C. W. Don, E. Minami, Y. W. Liu, J. J. Weyers, W. M. Mahoney, B. Van Biber, S. M. Cook, N. J. Palpant, J. A. Gantz, J. A. Fugate, V. Muskheli, G. M. Gough, K. W. Vogel, C. A. Astley, C. E. Hotchkiss, A. Baldessari, L. Pabon, H. Reinecke, E. A. Gill, V. Nelson, H. P. Kiem, M. A. Laflamme, and C. E. Murry, "Human embryonic-stem-cell-derived cardiomyocytes regenerate non-human primate hearts," *Nature,* vol. 510, pp. 273-7, 2014.
[54] N. Ferri, P. Siegl, A. Corsini, J. Herrmann, A. Lerman, and R. Benghozi, "Drug attrition during pre-clinical and clinical development: understanding and managing drug-induced cardiotoxicity," *Pharmacol Ther,* vol. 138, pp. 470-84, 2013.
[55] S. R. Braam, L. Tertoolen, A. van de Stolpe, T. Meyer, R. Passier, and C. L. Mummery, "Prediction of drug-induced cardiotoxicity using human embryonic stem cell-derived cardiomyocytes," *Stem Cell Research,* vol. 4, pp. 107-116, 2010.
[56] J. Zhang, G. F. Wilson, A. G. Soerens, C. H. Koonce, J. Yu, S. P. Palecek, J. A. Thomson, and T. J. Kamp, "Functional cardiomyocytes derived from human induced pluripotent stem cells," *Circ Res,* vol. 104, p. 12, 2009.
[57] C. Robertson, D. D. Tran, and S. C. George, "Concise Review: Maturation Phases of Human Pluripotent Stem Cell-Derived Cardiomyocytes," *Stem Cells,* vol. 31, pp. 829-837, 2013.

[58] S. Sheehy, P. Francesco, A. Grosberg, S. J. Park, Y. Aratyn-Schaus, and K. K. Parker, "Quality metrics for stem cell-derived cardiac myocytes," *Nature Biotechnology*, 2014.
[59] C. Kim, J. Wong, J. Wen, S. Wang, C. Wang, S. Spiering, N. G. Kan, S. Forcales, P. L. Puri, T. C. Leone, J. E. Marine, H. Calkins, D. P. Kelly, D. P. Judge, and H. S. Chen, "Studying arrhythmogenic right ventricular dysplasia with patient-specific iPSCs," *Nature*, vol. 494, pp. 105-10, 2013.
[60] G. Wang, M. L. McCain, L. Yang, A. He, F. S. Pasqualini, A. Agarwal, H. Yuan, D. Jiang, D. Zhang, L. Zangi, J. Geva, A. E. Roberts, Q. Ma, J. Ding, J. Chen, D. Z. Wang, K. Li, J. Wang, R. J. Wanders, W. Kulik, F. M. Vaz, M. A. Laflamme, C. E. Murry, K. R. Chien, R. I. Kelley, G. M. Church, K. K. Parker, and W. T. Pu, "Modeling the mitochondrial cardiomyopathy of Barth syndrome with induced pluripotent stem cell and heart-on-chip technologies," *Nat Med*, vol. 20, pp. 616-23, 2014.
[61] C. C. Gregorio and P. B. Antin, "To the heart of myofibril assembly," *Trends Cell Biol*, vol. 10, pp. 355-62, 2000.
[62] P. Helm, M. F. Beg, M. I. Miller, and R. L. Winslow, "Measuring and Mapping Cardiac Fiber and Laminar Architecture Using Diffusion Tensor MR Imaging," *Ann NY Acad Sci*, vol. 1047, pp. 296-307, June 1, 2005 2005.
[63] E. Ehler, *Cardiac Cytoarchitecture: How to Maintain a Working Heart*: Springer, 2015.
[64] P. L. Kuo, H. Lee, M. A. Bray, N. A. Geisse, Y. T. Huang, W. J. Adams, S. P. Sheehy, and K. K. Parker, "Myocyte shape regulates lateral registry of sarcomeres and contractility," *Am J Pathol*, vol. 181, pp. 2030-7, Dec 2012.
[65] P. Liao, D. Georgakopoulos, A. Kovacs, M. Zheng, D. Lerner, H. Pu, J. Saffitz, K. Chien, R.-P. Xiao, D. A. Kass, and Y. Wang, "The in vivo role of p38 MAP kinases in cardiac remodeling and restrictive cardiomyopathy," *Proceedings of the National Academy of Sciences*, vol. 98, pp. 12283-12288, October 9, 2001 2001.
[66] S. Kim, K. Ohta, A. Hamaguchi, T. Yukimura, K. Miura, and H. Iwao, "Angiotensin II induces cardiac phenotypic modulation and remodeling in vivo in rats," *Hypertension*, vol. 25, pp. 1252-9, 1995.
[67] J. Kim, J. Park, K. Na, S. Yang, J. Baek, E. Yoon, S. Choi, S. Lee, K. Chun, and S. Park, "Quantitative evaluation of cardiomyocyte contractility in a 3D microenvironment," *J Biomech*, vol. 41, pp. 2396-401, Aug 7 2008.
[68] J. Park, J. Ryu, S. K. Choi, E. Seo, J. M. Cha, S. Ryu, J. Kim, B. Kim, and S. H. Lee, "Real-Time Measurement of the Contractile Forces of Self-Organized Cardiomyocytes on Hybrid Biopolymer Microcantilevers," *Analytical Chemistry*, vol. 77, pp. 6571-6580, 2005/10/01 2005.
[69] P. Linder, J. Trzewik, M. Rüffer, G. M. Artmann, I. Digel, R. Kurz, A. Rothermel, A. Robitzki, and A. Temiz Artmann, "Contractile tension and beating rates of self-exciting monolayers and 3D-tissue constructs of neonatal rat cardiomyocytes," *Medical & Biological Engineering & Computing*, vol. 48, pp. 59-65, 2010/01/01 2010.
[70] J. N. Cohn, R. Ferrari, and N. Sharpe, "Cardiac remodeling—concepts and clinical implications: a consensus paper from an international forum on cardiac remodeling," *J Am Coll Cardiol*, vol. 35, pp. 569-582, 2000.
[71] M. S. Spach, J. F. Heidlage, P. C. Dolber, and R. C. Barr, "Electrophysiological effects of remodeling cardiac gap junctions and cell size: experimental and model studies of normal cardiac growth," *Circ Res*, vol. 86, pp. 302-11, 2000.

[72] I. W. Hamley, *Introduction to soft matter: synthetic and biological self-assembling materials*: John Wiley & Sons, 2013.
[73] D. Volfson, S. Cookson, J. Hasty, and L. S. Tsimring, "Biomechanical ordering of dense cell populations," *Proc Natl Acad Sci U S A,* vol. 105, pp. 15346-51, Oct 7 2008.
[74] P. W. Alford, A. W. Feinberg, S. P. Sheehy, and K. K. Parker, "Biohybrid thin films for measuring contractility in engineered cardiovascular muscle," *Biomaterials,* vol. 31, pp. 3613-21, May 2010.
[75] A. Krishnamurthy, C. T. Villongco, J. Chuang, L. R. Frank, V. Nigam, E. Belezzuoli, P. Stark, D. E. Krummen, S. Narayan, J. H. Omens, A. D. McCulloch, and R. C. P. Kerckhoffs, "Patient-specific models of cardiac biomechanics," *Journal of Computational Physics,* vol. 244, pp. 4-21, 2013.
[76] D. A. MacKenna, S. M. Vaplon, and A. D. McCulloch, "Microstructural model of perimysial collagen fibers for resting myocardial mechanics during ventricular filling," *Am J Physiol,* vol. 273, pp. H1576-86, 1997.
[77] A. Grosberg and M. Gharib, "Modeling the macro-structure of the heart: healthy and diseased," *Med Biol Eng Comput,* vol. 47, pp. 301-11, Mar 2009.
[78] J. Shim, A. Grosberg, J. C. Nawroth, K. K. Parker, and K. Bertoldi, "Modeling of cardiac muscle thin films: pre-stretch, passive and active behavior," *J Biomech,* vol. 45, pp. 832-41, Mar 15 2012.
[79] Benjamin M. Friedrich, A. Buxboim, Dennis E. Discher, and Samuel A. Safran, "Striated Acto-Myosin Fibers Can Reorganize and Register in Response to Elastic Interactions with the Matrix," *Biophys J,* vol. 100, pp. 2706-2715, 2011.
[80] M. A. Bray, S. P. Sheehy, and K. K. Parker, "Sarcomere alignment is regulated by myocyte shape," *Cell Motil Cytoskeleton,* vol. 65, pp. 641-51, Aug 2008.
[81] N. K. Drew, M. A. Eagleson, D. B. Baldo Jr, K. K. Parker, and A. Grosberg, "Metrics for Assessing Cytoskeletal Orientational Correlations and Consistency," *PLoS Comput Biol,* vol. 11, p. e1004190, 2015.